NASA CR-159527

NASA

INERT GAS THRUSTERS

Prepared for

LEWIS RESEARCH CENTER

NATIONAL AERONAUTICS AND SPACE ADMINISTRATION

GRANT NSG 3011

Annual Report

November 1978

Harold R. Kaufman
Department of Mechanical Engineering
Colorado State University
Fort Collins, Colorado

1. Report No. CR-159527	2. Government Accession No.	3. Recipient's Catalog No.
4. Title and Subtitle INERT GAS THRUSTERS		5. Report Date December 1978
		6. Performing Organization Code
7. Author(s) Harold R. Kaufman		8. Performing Organization Report No.
		10. Work Unit No.
9. Performing Organization Name and Address Department of Mechanical Engineering Colorado State University Fort Collins, Colorado 80523		11. Contract or Grant No. NSG-3011
12. Sponsoring Agency Name and Address National Aeronautics and Space Administration Washington, D.C. 20546		13. Type of Report and Period Covered Contractor Report
		14. Sponsoring Agency Code

15. Supplementary Notes

Grant Manager, Vincent K. Rawlin
NASA Lewis Research Center
Cleveland, Ohio 44135

16. Abstract   Inert gas thrusters have continued to be of interest for space propulsion applications. Xenon is of interest in that its physical characteristics are well suited to propulsion. High atomic weight and low tankage fraction are major factors in this choice. If a large amount of propellant is required, so that cryogenic storage is practical, argon is a more economical alternative. Argon is also the preferred propellant for ground applications of thruster technology, such as sputter etching and deposition. Additional magnetic field measurements are reported herein. These measurements should be of use in magnetic field design.

The diffusion of electrons through the magnetic field above multipole anodes has been studied in detail. The data are consistent with Bohm diffusion across a magnetic field. The theory based on Bohm diffusion is simple and easily used for diffusion calculations. Limited startup data were obtained for multipole discharge chambers. These data were obtained with refractory cathodes, but should be useful in predicting the upper limits for starting with hollow cathodes.

Discharge-chamber performance was obtained for a multipole discharge chamber operating with a hollow cathode. Discharge losses and utilizations were generally similar to those obtained with refractory cathodes, but the losses were 100-200 eV/ion lower. The higher losses with the refractory cathodes were believed due mostly to poor placement of these cathodes. The discharge voltage generally tended to decrease with either higher main-cathode flow rates or higher total discharge-chamber flow rates. These results are consistent with previous mercury-propellant experience. Limited doubly charged ion data were also obtained. To the extent that comparison was possible, these data were in agreement with similar data obtained with a refractory cathode.

Hollow cathode data were also obtained. These data indicated that in a bell jar the anode area is a more critical factor with argon and xenon than with mercury. Calculations of the ion drift with the neutral flow out a hollow cathode orifice support the viewpoint that ions are carried from the orifice against the local electric field by ion-atom collisions to the plume region when operation is in the spot mode. A correlation parameter based on this picture has similarities to another correlation parameter derived previously. A flow control is described in sufficient detail to permit duplication. The flowmeter and control valve used in this flow control both use concepts well suited for eventual development into space flight hardware.

17. Key Words (Suggested by Author(s)) Electrostatic thruster Ion thruster Ion source	18. Distribution Statement Unclassified-Unlimited

19. Security Classif. (of this report) Unclassified	20. Security Classif. (of this page) Unclassified	21. No. of Pages	22. Price*

TABLE OF CONTENTS

LIST OF FIGURES

I   INTRODUCTION

Inert gas thrusters have continued to be of interest for space propulsion applications.   Xenon is of interest in that its physical characteristics are well suited to propulsion.   High atomic weight and low tankage fraction are major factors in this choice.   If a large amount of propellant is required, so that cryogenic storage is practical, argon is a more economical alternative.   Argon is also the preferred propellant for ground applications of thruster technology, such as sputter etching and deposition.

This report covers the progress made in inert-gas thruster technology since the last annual report.[1]   Progress is reported in the areas of magnetic field design, diffusion of electrons to anodes, starting, discharge-chamber performance, hollow cathodes, and propellant flow control.   Because argon represents a larger departure than xenon from previous experience with mercury or cesium, performance with argon is emphasized over that with xenon.   SI (rationalized mks) units are used in this report unless otherwise indicated.

II MAGNETIC FIELD MEASUREMENTS

Magnetic field measurements were made during the investigation of the various discharge-chamber operating limits. These measurements should be of interest to designers of multipole chambers.

A typical demagnetization curve for Alnico V is shown in Fig. 2-1.[1] Alnico V is the customary choice for discharge-chamber magnets because it is readily available in a large range of sizes, has a high flux density, and can withstand temperatures up to about 500°C with only a moderate ($\simeq$ 10%) loss in strength. There are more exotic magnet materials that have more resistance to demagnetization, but with the low field strengths required for discharge chambers, this added resistance does not appear necessary.

The total magnetic flux between pairs of pole pieces was integrated for 7.5-cm,[2] 15-cm,[3] and 30-cm[4] multipole discharge chambers. Different numbers of magnets were also used for the 7.5-cm and 15-cm chambers. As shown in Fig. 2-2, the results clearly fell into two groups, the 30-cm measurement and the rest of the measurements. This difference is attributed to the difference in magnet preparation. The magnets were all cut from 6.3 mm diameter stock, and were about 2.5 cm long. The magnets for the 30-cm source were cut to length using a cut-off wheel and then ground flat, with considerable heating and vibration. The 7.5-cm magnets were also cut to length in this manner, but were remagnetized using a simple direct-current solenoid for the remagnetizing. The 15-cm magnets were purchased cut to length and magnetized by the manufacturer. As is shown in Fig. 2-2, the remagnetized magnets performed essentially the same as those cut to length and magnetized by
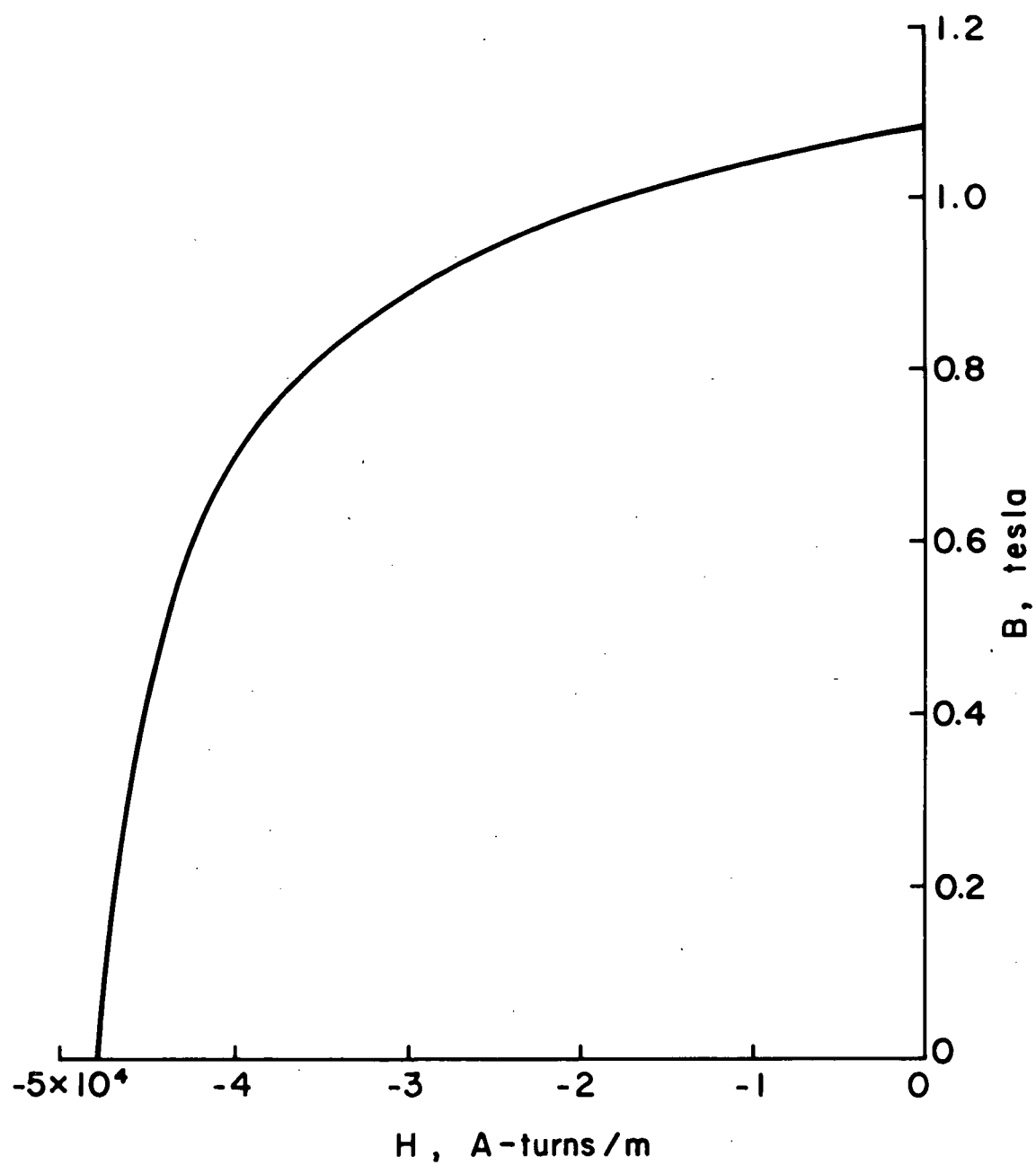
Figure 2-1. Demagnetization curve for Alnico V.
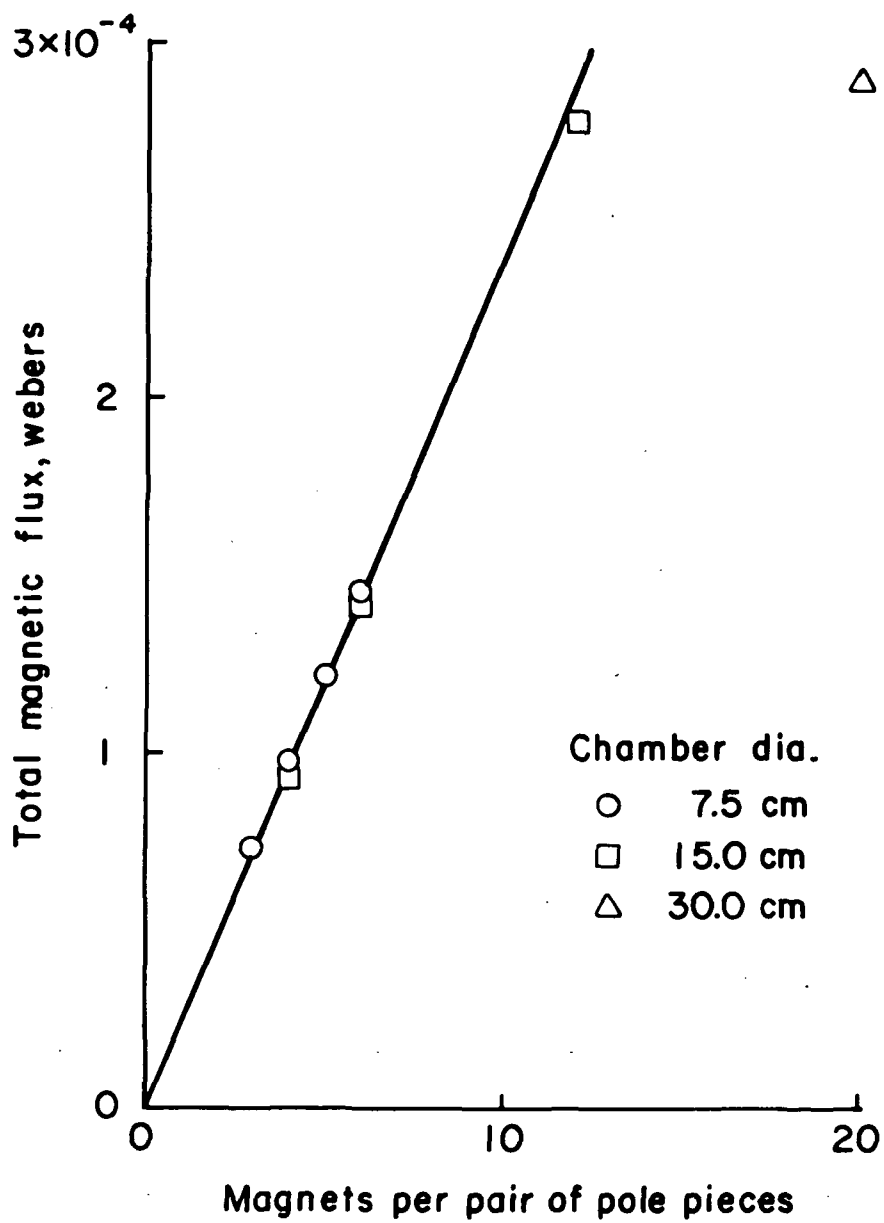
Figure 2-2. Integrated flux of 6.3-mm diameter Alnico V
            magnets, with a length of 25.4 mm.

the manufacturer. The slope of the line shown for this group is 2.4 x 10^{-7} webers/magnet. The 30-cm point corresponds to about 1.45 x 10^{-7} webers/magnet, or about 60% of the mean flux per magnet of the other group.

An obvious and unoriginal conclusion concerning Fig. 2-2 is that poor handling and/or fabrication techniques can adversely affect permanent magnet performance. The results of Fig. 2-2 can also be compared with Fig. 2-1. An isolated magnet experiences a demagnetizing effect that is a function of its length-to-diameter ratio. The magnets used all had a ratio close to 4:1. This ratio for an isolated Alnico V magnet corresponds to approximately the knee of the demagnetization curve in Fig. 2-1. The flux of 2.4 x 10^{-4} webers through a magnet diameter of 6.3 mm is a flux density of 0.77 tesla, which also corresponds to the knee of Fig. 2-1.

The amount of demagnetization an isolated magnet undergoes is an important design consideration. If a magnet is demagnetized beyond (to the left of) the knee of Fig. 2-1, much of the flux capability will be lost without remagnetization. It is often possible to remagnetize such a magnet once it is installed in a magnetic circuit, but unless the magnet can be isolated without large demagnetization, this remagnetization would be required with every disassembly and reassembly. As mentioned above, the 4:1 length-to-diameter ratio corresponds (when a magnet is isolated) to about the demagnetization knee for Alnico V. A smaller length-to-diameter ratio will suffer a larger demagnetization and should be avoided. On the other hand, a larger ratio will show only a small improvement over the knee value. The demagnetization is almost always more severe for an isolated magnet than for one installed in

a thruster, so that the isolated condition is the limiting one. Thus
length-to-diameter ratios of Alnico V should be limited to about 4:1,
or larger.

Pole-piece curvature is typically one of two kinds, as indicated
in Fig. 2-3. The curvature of the upstream pole pieces, shown in
Fig. 2-3(a), appears to have little effect on the magnetic field. When
the number of magnets were adjusted to give nearly constant field
integrals above the anodes, the ratio of magnet number to anode length
was found to be constant within 5% for most anodes.[4] The implication
is that the curvature of the magnetic field can be ignored for this
direction of curvature if anode length is used as a basis of comparison.
That is, the effect of a shorter pole piece near the axis of the
thruster is substantially balanced by the effect of the longer pole
piece farther from the axis.

The curvature of side-wall pole pieces, shown in Fig. 2-3(b), is
less straightforward. The decreased space on the inside of the thruster,
compared to outside, can result in a significant shift in flux. This
effect is shown in Fig. 2-4 for the fraction of flux inside the mean
radius. The point for zero D/R_m is a theoretical one. (If the curva-
ture is vanishingly small, one would expect exactly half the flux to
fall inside the mean radius.) The other points are (in order of in-
creasing D/R_m) from the 30-cm, 15-cm, and 7.5-cm discharge chamber.
Only one point (with limited accuracy) was available from the 30-cm
chamber. Multiple points were available for both the 15-cm and 7.5-cm
chambers. Fig. 2-4 clearly shows that the reduced space within the
chamber results in more flux being shifted to the outside, as curvature
is increased. The space reduction within the thruster also results in
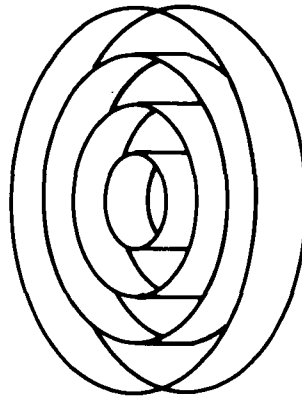
(a) Upstream end
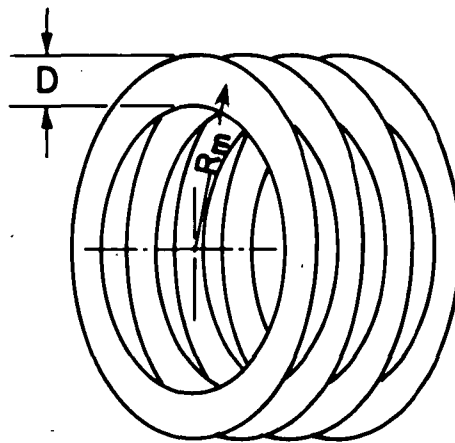
(b) Side walls

Figure 2-3. Pole-piece curvature.
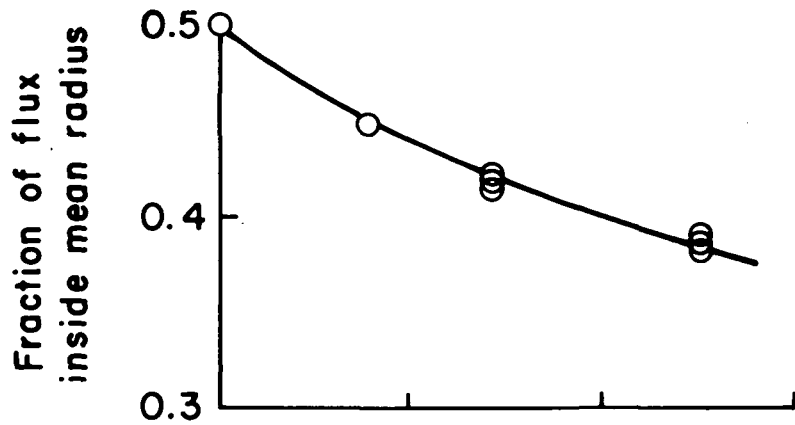
(a) Magnetic flux inside mean radius.

Pole-piece width ratio, D/R_m
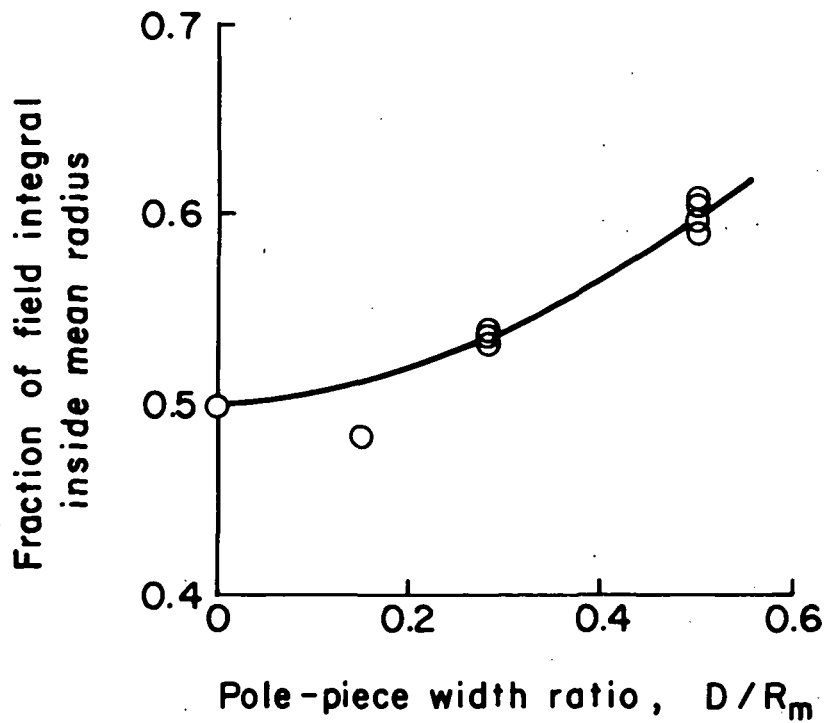
(b) Magnetic integral inside mean radius.

Figure 2-4. Effect of side wall curvature on magnetic field.

an increase in field strength at that location. This increase results in the field integral ($\int Bdx$) being larger inside the mean radius than it is outside. Since it is the field integral that controls the primary electron containment, the effect of this curvature should be included in multipole magnetic design.

III ANODE AREA LIMITATION

The electron current to a discharge-chamber anode can be limited by the diffusion of electrons through the magnetic field above the anode. This condition can be thought of as either an anode area limitation or a limitation on current (or current density) to that anode. The current approach is more convenient for derivation of the effect, while considering it as an area effect appears more useful in discussing experimental performance. The effect is discussed primarily in connection with the multipole magnetic field. The effect, though, appears to be involved wherever electrons must cross magnetic field lines to reach a discharge-chamber anode. The development of this theory for the multipole magnetic-field configuration is facilitated by the ease with which that configuration can be analyzed.

Before presenting the theory of this effect, it should be emphasized that the anode area involved may, or may not, be a physical area. The electron mobility along magnetic field lines is much greater than the mobility across field lines. The effective anode area is therefore that area from which electrons can be drained from the discharge plasma by moving along field lines to reach the anode.

Electron Diffusion Theory

Electrons emitted from the cathode, together with electrons liberated in the ionization process, must diffuse to the anodes to sustain a discharge. In doing so, the electrons must cross magnetic fields sufficient to contain electrons of primary energy. The basic equation for electron diffusion in the presence of voltage and density gradients is

$$\vec{\Gamma} = -\mu \, n_e \vec{E} - D\vec{\nabla}n_e \qquad (3-1)$$

where $\vec{\Gamma}$ represents the particle flux of electrons, n_e is the electron number density, and μ and D are the electron mobility and diffusion coefficients respectively. The mobility and diffusion coefficients are related by the Einstein relation,

$$\mu = e \, D/kT \qquad (3-2)$$

where e is absolute magnitude of the electronic charge, k is Boltzmann's constant and T is the electron temperature. The classical diffusion coefficient in the absence of (or parallel to) a magnetic field is

$$D = kT_e/m_e\nu_e \qquad (3-3)$$

with m_e the electron mass and ν_e the electron collision frequency.

The classical diffusion coefficient normal to a magnetic field is

$$D_\perp = D/(1 + \omega^2\tau^2) \qquad (3-4)$$

where ω is the electron cyclotron frequency and τ is the mean time between collisions ($\tau = \frac{1}{\nu_e}$). This reduces in the strong field limit of $\omega\tau \gg 1$ to

$$D_\perp = D_e/\omega^2\tau^2 = kT_e \, m_e\nu_e/e^2B^2 \qquad (3-5)$$

There is also a drift velocity at right angles to the applied field $\vec{E}$. For the last diffusion coefficient to be observed, this drift must take place without generating an additional electric field. Anodes and pole pieces that are closed loops meet this condition.

Experimental measurements of electron diffusion across a magnetic field with $\omega\tau \gg 1$ usually correspond to larger diffusion coefficients than Eq. (3-5), often by orders of magnitude. These larger values are

attributed to "anomalous" or "turbulent" diffusion. A simple and well known semiempirical approach to turbulent electron diffusion was given by Bohm.[1] The Bohm diffusion coefficient given in later publications[2,3] has a slightly different numerical coefficient and is

$$D_B = kT_e/16 \, eB \ . \tag{3-6}$$

Bohm diffusion varies as $1/B$, while classical diffusion for the same strong field condition varies as $1/B^2$. In fact, the Bohm value of diffusion is obtained if we assume that turbulence increases the effective collision frequency to $\omega/16$. Despite the apparent simplicity of the Bohm diffusion coefficient, it effectively correlates experimental observations over a wide range of conditions.[3]

It should be noted that the diffusion of interest herein is primarily of Maxwellian electrons. Whether we are concerned with the coulomb collisions of classical diffusion or the collective collisions of turbulent diffusion, the lower energy electrons have almost all the collisions, hence diffuse across a magnetic field preferentially compared to higher energy primary electrons.

The diffusion condition for anodes that we are most interested in is the maximum diffusion that can be obtained without the assistance of a forward electric field, which would result if the anodes were substantially more positive than the discharge-chamber plasma. A reasonable assumption for this limiting condition appears to be zero electric field in the region of interest close to the anodes of a multipole discharge chamber. This condition of nearly uniform potential in the diffusion region has been observed experimentally,[4] with the only nonuniform region a jump of several

volts at the anode. Using this uniform potential assumption together with the Bohm diffusion coefficient, Eq. (3-1) can be written in one dimension as

$$\Gamma x = -D_B \ dn_e/dx \ .$$ (3-7)

In terms of current density, this becomes

$$j = e \ D_B \ dn_e/dx \ .$$ (3-8)

With the substitution of Eq. (3-6), we find

$$j = \frac{kT_e}{16B} \frac{dn_e}{dx} \ .$$ (3-9)

We do not assume prior knowledge of the variation of n_e with x. Instead, we use the near constancy of current density in the diffusion region, which results from the small thickness of that region compared to chamber diameter and the small fraction of total ionization therein. Noting also that the electron temperature is also nearly constant in the diffusion region,[4] we collect all the constants of Eq. (3-9) on the left side to obtain

$$\frac{16j}{kT_e} = \frac{dn_e}{Bdx} \ .$$ (3-10)

We still do not know details of the variation of n_e with x, but we can replace the differential expressions with integral expressions

$$\frac{dn_e}{Bdx} = \frac{n_e}{\int Bdx} \ ,$$ (3-11)

where $\int Bdx$ is the same integral that is involved in the containment of high-energy primary electrons.[5] With this substitution, the electron current density becomes

$$j = \frac{kT_e \, n_e}{16 \int Bdx} \quad . \tag{3-12}$$

In calculating this current density, the fringe field area above the anodes is important, while the projected area of the anodes is not. As mentioned at the beginning of this section, this is because the diffusion coefficient parallel to the magnetic field is so much greater than that normal to the field. The absence of any significant effect of anode projected area was also established experimentally.[6]

An additional correction can be made for the variation in fringe-field area normal to j. The magnetic field lines close to the inner anode edges follow paths nearly parallel to the smoothed outer surface of the discharge chamber (see dashed line in Fig. 3-1). Farther away from the anodes, though, the field lines follow longer looping paths. This variation in field line length ℓ_B results in a similar variation in area normal to the diffusing electron current. A numerical integration through increments of $\int Bdx$ can be used to correct for this area variation. An applicable equation is

$$j = \frac{kT_e}{16} \frac{\sum\limits_{i=1}^{N} \Delta n_{e_i}}{\sum\limits_{i=1}^{N} \Delta \int Bdx_i \; d/\ell_{B_i}} \quad , \tag{3-13}$$

where Δn_e is the increment in electron density required to drive current density j through an increment in magnetic field integral $(\Delta \int Bdx)_i$ with the "area" ℓ_{B_i}. The length ℓ_{B_i} is effectively an area because a unit width is assumed in the direction normal to both ℓ_{B_i} and j. The local current density thus equals j where $\ell_{B_i}/d = 1$. Solving Eq. (3-13) is facilitated if one recognizes the clear analogy with current flow through
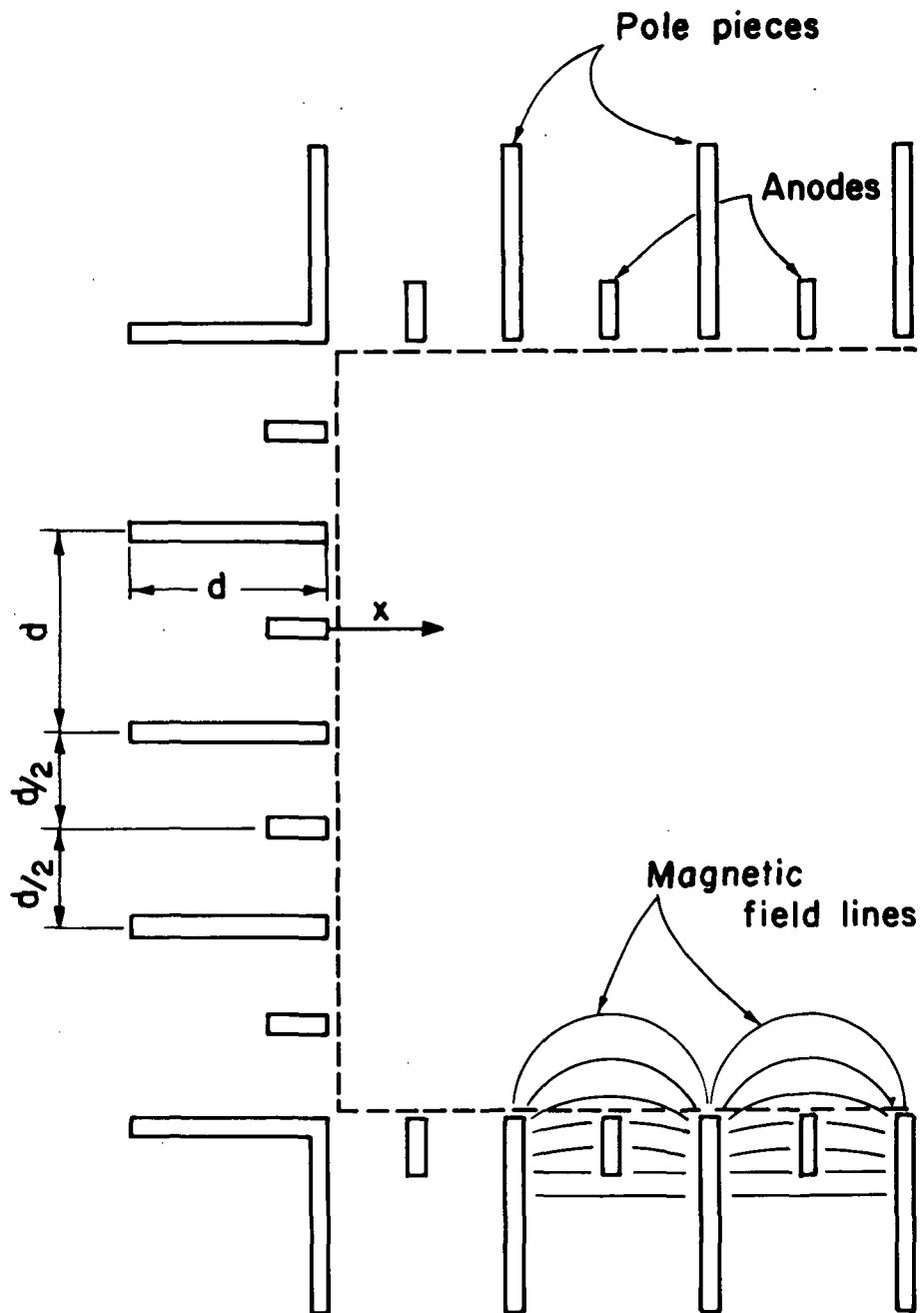
Figure 3-1. Multipole discharge chamber. Dashed line
shows assumed outer surface of discharge
chamber.

resistors connected in series. In this analogy, the increment Δn_e
is analogous to the voltage across a resistor, while the resistance is
analogous to $(\Delta \int Bdx)_i \; d/\ell_{B_i}$. Using this analogy, it can be shown that
an effective overall value of ℓ_{B_i}/d is

$$\frac{\ell_{B_{eff}}}{d} = \frac{\int Bdx}{\int B\frac{d}{\ell_B(x)} \, dx} \tag{3-14}$$

where the integral is over the region between the anode and the nearly
field-free main volume of the discharge chamber. We can use a curve fit
for the variation of B with distance similar to one obtained previously,[5]

$$B = B_{max} \exp[-1.5 \; (x/d + 1/2)^2] \; , \tag{3-15}$$

where x is indicated in Fig. 3-1. Assuming parabolic arc paths for field
lines between the ends of pole pieces, one can then find by integrating
Eq. (3-14) that the area correction is equivalent to

$$j \approx \frac{kT_e \; n_e}{13 \int Bdx} \tag{3-16}$$

where j is based on the area indicated by the dashed line in Fig. 3-1.
Equation (3-16), then, can be used to find the maximum electron current
that will diffuse to the anodes without making the anodes more positive
than the discharge-chamber plasma. In view of the relatively small
difference between Eqs. (3-12) and (3-16), a more accurate correction
for the area affect does not appear necessary. Also, a separate correc-
tion for corner pole pieces, which have a slightly different variation
of B with x, is not required.

Comparison with Experimental Results

The first comparison is with data obtained using the 30-cm multipole discharge chamber (configuration described in ref. 5). This discharge chamber was operated using different numbers of anodes connected to the positive potential of the discharge supply. The plasma was initially close to anode potential with all the anodes connected. As sufficient anodes were disconnected, the plasma assumed a potential substantially negative of the anodes. This effect is shown with minor differences in Figs. 3-2(a) and 3-3(a). Fig. 3-2 was obtained at close to the minimum discharge voltage for each anode configuration, while Fig. 3-3 was obtained about 10 V higher. These operating conditions were determined by operating at a constant discharge current and decreasing discharge voltage. The two propellant densities shown in each figure cover the usual range of interest for thruster operation. When the effective anode area (proportional to active anode length) is reduced below an approximate critical value, the plasma potential apparently must become increasingly negative of the anodes to maintain the desired electron current to the anodes. Because electron diffusion can result from both potential and density gradients, the added contribution of the potential gradient is the amount required to compensate for the reduced anode area.

The theoretical electron currents to the anodes were calculated using Eq. (3-16), the effective anode areas for the active anodes, and plasma properties from a centrally located Langmuir probe. The experimental anode currents were assumed to be the sums of discharge (emission) and beam currents. The ratios of experimental-to-theoretical anode currents were then plotted in Figs. 3-2(b) and 3-3(b). Basing the calculations on the plasma properties led to considerably more scatter in the (b) portions of
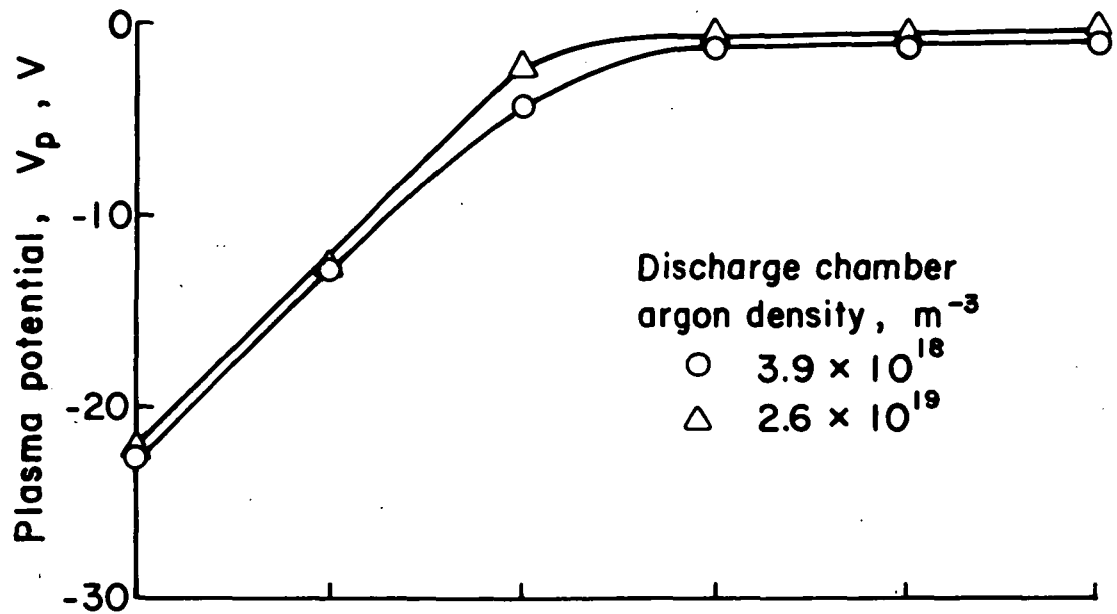
(a) Plasma potential
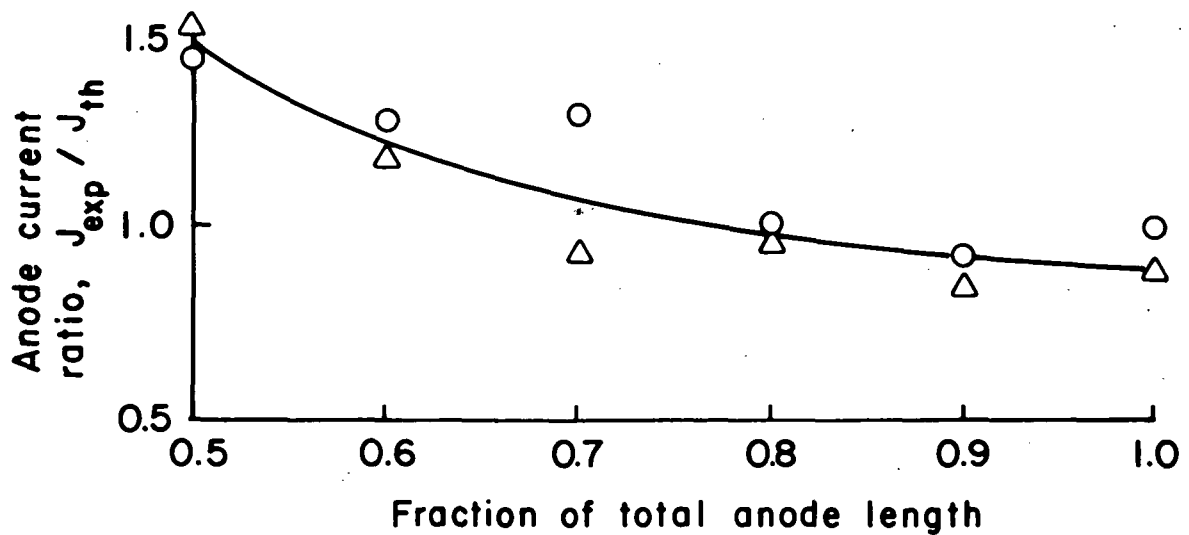
(b) Experimental - to - theoretical anode current ratio

Figure 3-2.   Plasma and anode parameters near the minimum
               discharge voltage.
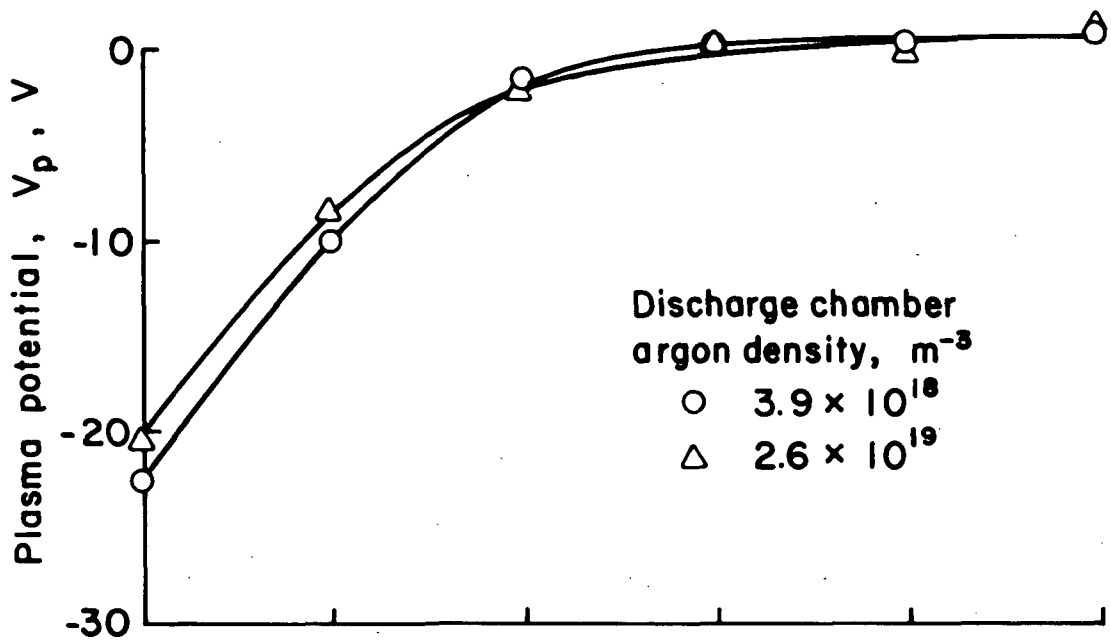
(a) Plasma Potential
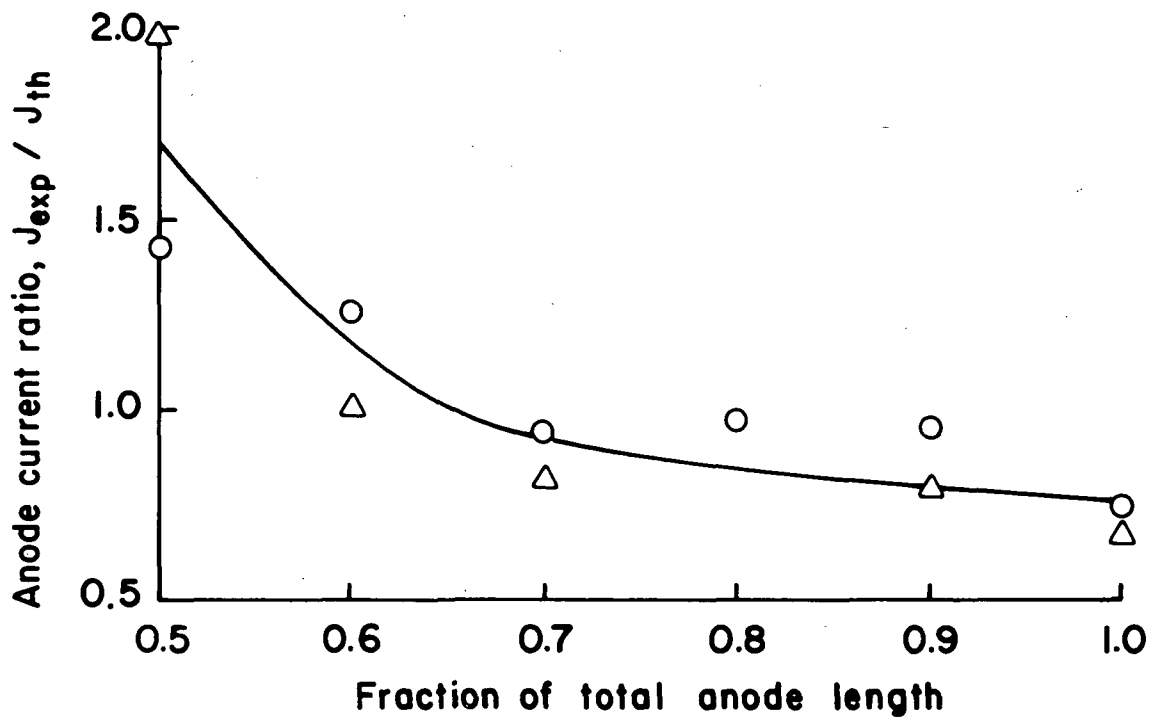
(b) Experimental-to-theoretical anode current ratio

Figure 3-3. Plasma and anode parameters at about 10V above minimum discharge voltage.

Figs. 3-2 and 3-3 than in the (a) portions, enough scatter so that only one curve is shown in each (b) portion. Still, the trends appear clear. The anode current ratio, J_{exp}/J_{th}, becomes greater than unity at close to the anode fraction where the plasma becomes negative of the anodes.

Operation with a plasma significantly negative of the anodes is believed to be marginally stable, or even unstable. The reasons for such a viewpoint are the absence of such data in thruster literature,* and the difficulty of obtaining such data in this investigation. The data of Figs. 3-2 and 3-3 were obtained by using rheostats to gradually disconnect anodes, thereby minimizing switching transients. Without these rheostats, switching of anodes without extinguishing the discharge was reliable only

---

* The only literature description of a plasma significantly negative relative to the anode is the cesium multipole of Moore.[7] A very high magnetic field strength was used in this early multipole design. This high field strength apparently prevented sufficient electrons from diffusing to the multipole anodes, which roughly resembled the multipole anodes of Fig. 3-1. A "plasma anode" (a narrow strip of metal across the discharge chamber, unprotected by a magnetic field) was therefore introduced to provide a path for the required electron current. Stable operation with the plasma negative relative to the multipole anodes was obtained by also operating the plasma anode negative of the multipole anodes. The plasma anode, of course, operated close to plasma potential. Similar operation may have been used by Ramsey,[8] but insufficient description was included for the determination of the potential bias between plasma and multipole anodes.

above ~70% of total anode length.[5] That is, it was reliable only at anode lengths where the plasma was not significantly negative of the anodes.

Other tests were also conducted with both 15-cm and 7.5-cm multipole discharge chambers (configurations described in refs. 9 and 10). Because plasma probe data were not obtained with these smaller discharge chambers, it was necessary to estimate electron temperature from other tests and electron density from beam current. To the latter end, the beam current extracted can be expressed as

$$J_b = A_{scr} \, n_e \, v_B \, e \, , \qquad\qquad (3\text{-}17)$$

where n_e is the electron/ion density, v_B is the Bohm critical sheath velocity, e is the absolute electronic charge, and A_{scr} is the effective open screen area for extraction. This area can be somewhat above or below the geometrical open area, but the latter should be a good approximation. Replacing the Bohm velocity with the equivalent expression $(k \, T_e/m_i)^{\frac{1}{2}}$, Eq. (3-17) becomes

$$J_b = A_{scr} \, n_e \, e \, (kT_e/m_i)^{\frac{1}{2}} \, . \qquad\qquad (3\text{-}18)$$

using K_{ab} as the anode-to-beam current ratio, the anode current required to generate the ion beam can be written as

$$J_a = K_{ab} \, A_{scr} \, n_e \, e \, (kT_e/m_i)^{\frac{1}{2}} \, . \qquad\qquad (3\text{-}19)$$

From Eq. (3-16), the current permitted to diffuse to the anode (or anodes) without the anode becoming substantially more positive than the discharge-chamber plasma is

$$J_a = A_a \, kT_e \, n_e/13\!\int\! Bdx . \qquad\qquad (3\text{-}20)$$

Equating these two anode currents to obtain the minimum anode area for stable operation,

$$A_a = 13 \; K_{ab} \; A_{scr} \; e \int Bdx / (kT_e \; m_i)^{\frac{1}{2}} \; . \qquad (3\text{-}21)$$

This, then, is the relationship that can be used in the absence of plasma probe data.

In earlier tests of the 15-cm discharge chamber with argon[6] the mean electron temperature ranged from about 5 to 15 eV. Using 10 eV as a typical value, together with measured values for the magnetic field integral, screen open area, and anode-to-beam current ratio at the minimum discharge voltage,* Eq. (3-21) was used to estimate anode area. For a 48 magnet configuration of the 15-cm chamber, an anode area of 390-570 cm^2 was estimated; while for a 24 magnet configuration an anode area of 430-510 cm^2 was estimated. The measured anode area was 471 cm^2, which is in excellent agreement with the estimates from Eq. (3-21).

Similar minimum discharge voltage tests were conducted with the 7.5-cm discharge chamber. Inasmuch as electron temperature generally increases as thruster size becomes smaller, an electron temperature of 15 eV was felt to be a better estimate for this thruster size. With this temperature

---

* The minimum discharge voltage, where the discharge is extinguished, is believed to correspond to the anode diffusion limit. The reason that the limit is approached in this condition is that the discharge losses per ion are roughly constant while the discharge voltage decreases toward the limit. As a result, the ratio of anode-to-beam current, K_{ab}, increases as discharge voltage drops. When K_{ab} increases to a large enough value, at the minimum voltage, the required anode area will exceed the actual anode area and the discharge will extinguish.

and similar measured values as for the 15-cm tests, Eq. (3-21) indicated

an anode area of 70-130 cm^2. The measured anode area was 118 cm^2, which

again is in excellent agreement.

As mentioned earlier in this section, the diffusion theory presented

appears to be applicable wherever electrons must cross magnetic field

lines to reach a discharge-chamber anode. For example, we can apply this

theory to mildly divergent magnetic field thrusters. Because the magnetic

field lines of such a thruster do not follow long looping paths, a constant

of 16 should replace the constant of 13 in Eq. (3-21). With this change,

a Maxwellian electron temperature of 5 eV, the atomic weight of mercury,

a moderate magnetic-field integral of 75 x 10^{-6} Tesla-m, and a typical

anode-to-beam current ratio of 11, the minimum ratio of A_a/A_{scr} is about 4.

For the usual 50% open screen of early thrusters, this ratio translates

into a minimum anode that is about twice the total beam area. Or expressed

somewhat differently, a minimum length-to-diameter ratio of about 0.5 for

the discharge chamber. This result is in qualitative agreement with obser-

vations of early thrusters, where a length-to-diameter ratio of unity, or

slightly less, showed stable operation. Shorter chambers, though, were

hard to start and tended to extinguish easily.

This diffusion theory also appears applicable to general performance

trends. As an example, the minimum permissible discharge voltage tends

to increase as neutral pressure in the discharge chamber is decreased.

We also know that, in most operating ranges of interest, the discharge

losses tend to increase as neutral density is decreased. This increase

would result in an increase in required anode current at constant discharge

voltage, which, in itself, would result in an increased requirement for

anode area. If this increased anode area is not available, then the minimum discharge voltage increases to where the anode current becomes consistent with the anode area available.

As another example of showing performance trends, operation with lighter gases has been observed to result in more difficulty in maintaining a discharge, usually with higher minimum discharge voltages. We know that electron temperature usually increases somewhat with lighter ion masses, but not as rapidly as the mass decreases. From Eq. (3-21), then, the net effect of electron temperature and ion mass changes should be to require more anode area for a lighter gas. This result is consistent with the observed operational problems described above.

The electrostatic containment of ions (to reduce required discharge losses) was proposed by Moore[7] and Ramsey.[8] Although a significant fraction of the anodes were operated substantially positive of the discharge-chamber plasma in the multipole tests described earlier, no decrease in discharge losses was noted. The explanation appears to be that the turbulence expected with Bohm diffusion is probably sufficient to scatter a significant number of ions into the anodes and pole pieces despite the average adverse electric field. The concept of electrostatic containment thus appears to be offset, at least in part, by the effects of plasma turbulence.

Application to Design

The electron diffusion theory of this section can be applied to design problems. An obvious application is to estimate the minimum required anode area for expected operating conditions. Less obvious, is the evaluation of other multipole magnetic field configurations.

One example of a possible design is shown in Fig. 3-4(a). This flux concentrator design has been suggested in the past as a means of reducing the stray magnetic flux, thereby reducing the required magnet weight. From the theory herein, the flanges that serve to concentrate the flux will also serve to reduce the effective anode area. Inasmuch as the flux integral above the anode is fixed by the need to contain high velocity primary electrons, this integral will need to be about the same for both the regular design and the design of Fig. 3-4(a). The reduction of magnet weight would thus have to be balanced against the loss in effective anode area.

Another approach, the recessing of anodes behind the pole pieces, is shown in Fig. 3-4(b). The theory clearly indicates that the shape of the field above the anodes is of secondary importance. Except for corner locations, the anodes have in the past been made flush with the inside edges of the pole pieces. By recessing the anodes, it should be possible to reduce the number of magnets for the same magnetic integral above the anodes.

As a final comment, the diffusion theory presented herein assumes continuous paths (closed loops) for electron drift velocity normal to any applied electric field. For the observed magnitude of Bohm diffusion, this drift velocity is about 16 times the diffusion velocity in the direction of the applied electric field. This means that, in the presence of an electric field near anodes, the electron drift velocity parallel to the anodes is much greater than the diffusion velocity toward the anodes. When the drift velocity path is interrupted, an electric field is produced normal to the original electric field, which greatly increases electron diffusion due to the original electric field.
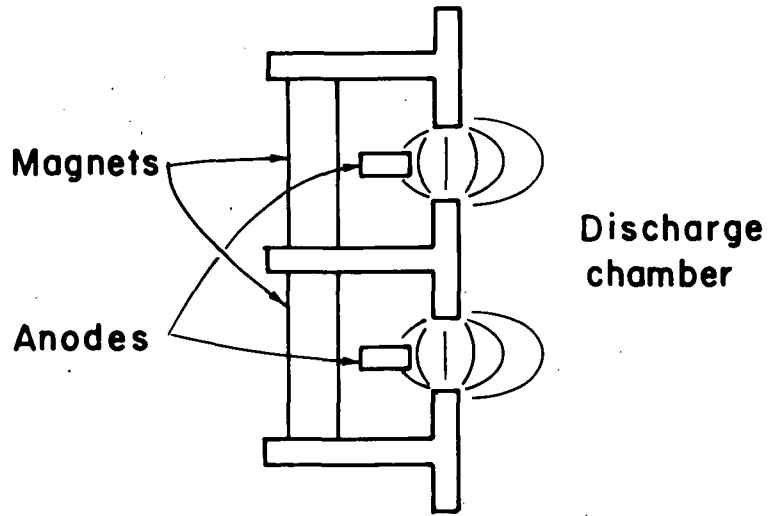
(a) Flux concentration
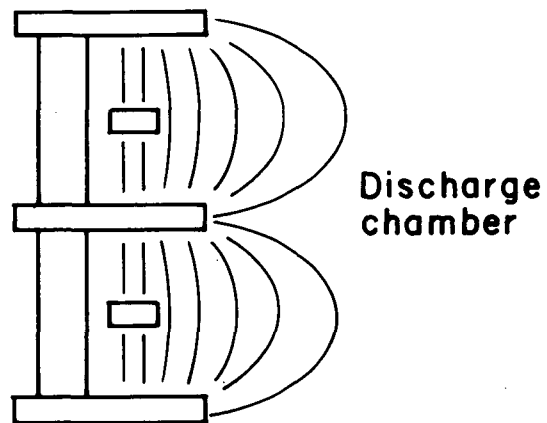
(b) Recessed anodes

Figure 3-4. Possible multipole magnet and pole-piece
configurations.

Translated into multipole anode design, interrupted drift paths should greatly increase the desired diffusion of Maxwellian electrons, presumably easing area limits for the anode as well as reducing minimum discharge voltages.

Discharge chamber starting voltages were obtained along with the
electron diffusion data presented in the preceding section. The type
of cathode is not significant for electron diffusion data, but can have
an effect on starting voltages. Specifically, a hollow cathode, because
it generates a plasma in addition to emitting electrons, would be expected
to result in somewhat lower starting voltages. Refractory metal cathodes
were used in these tests. The starting voltages of this section should
therefore be considered the upper limits of what might be expected using
hollow cathodes. The transition to a normal discharge at lower voltage
proceeds rapidly once the current exceeds a few mA. All the data presented
were also obtained using argon propellant and with high voltage power supplies
(beam and accelerator) turned off. The required starting voltages for the
discharge chamber would have been higher if the high voltage supplies had
been left on.

Different anode configurations were involved in the 7.5,[1] 15,[2] and
30[3] cm discharge chambers tested. Before comparing these different cham-
bers, then, it is of interest to find out the effect of anode configuration
within a single chamber. The data for this effect is shown in Fig. 4-1.
As shown, there is no substantial or consistent trend of starting voltage
with the fraction of total anode length connected to the discharge supply.
From these and other tests, it appeared that anode configuration was not
important unless the minimum voltage to maintain a discharge approached
the starting voltage.

The starting data for the three discharge chambers tested are shown
in Fig. 4-2. The neutral densities shown were calculated from ambient
pressures, together with propellant flow rates and effective open areas
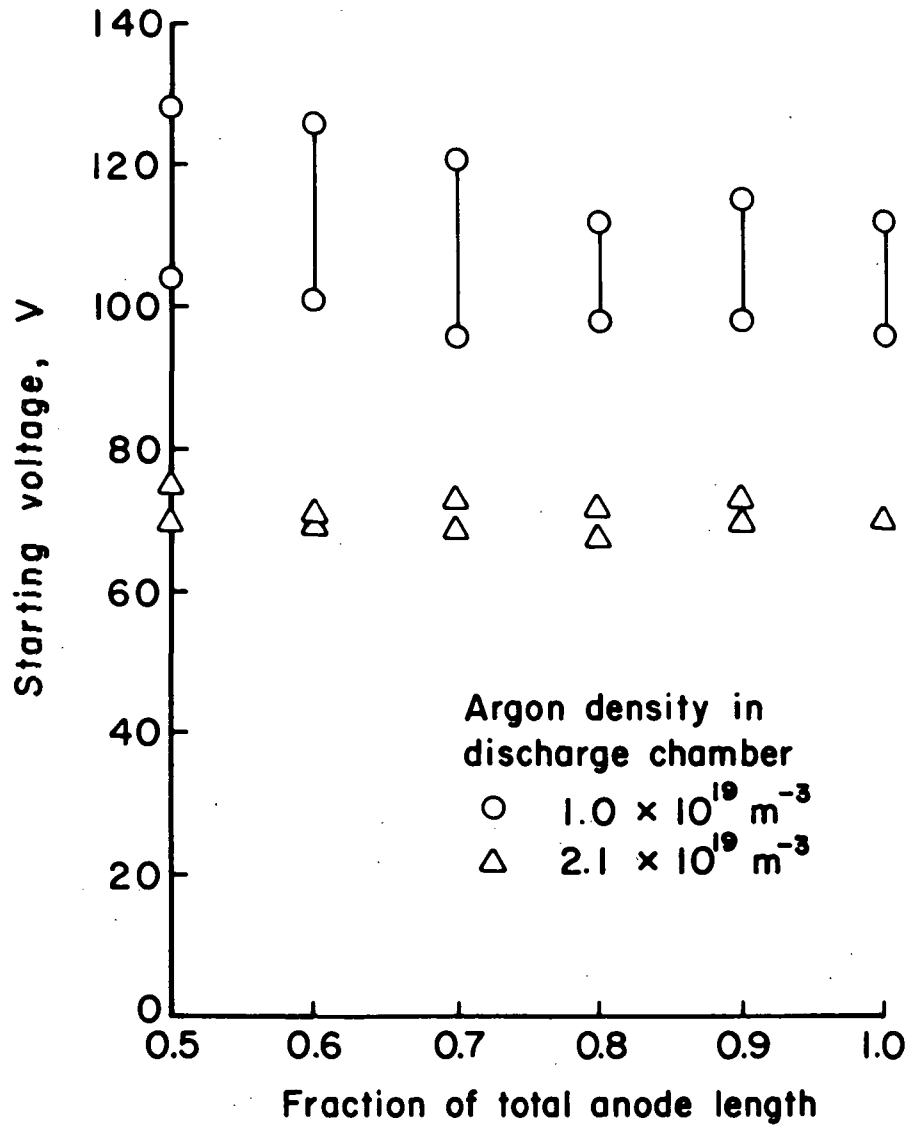
Figure 4-1. Effect of anode length on starting voltage
for a 30-cm multipole thruster.
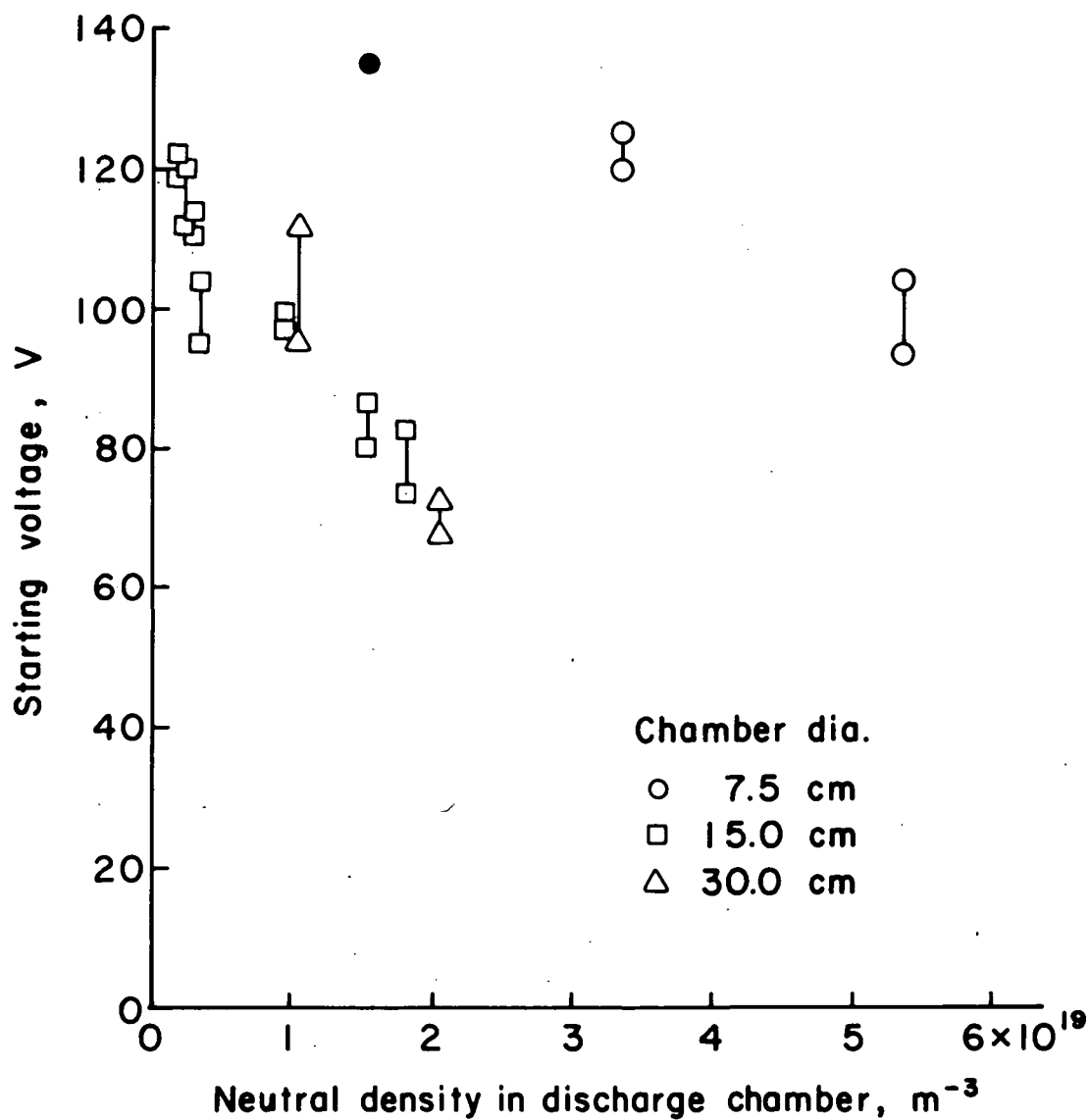
Figure 4-2. Starting voltages as a function of neutral density for three different discharge chambers. (The solid point represents no start with maximum power supply voltage.)

of the accelerator systems.* For comparison with ion gauge readings, the maximum density tested corresponded to about 1.6×10^{-3} Torr. The small 7.5 cm chamber clearly showed a shift to higher neutral densities for the same starting voltages. There was no comparable separation between 15 and 30 cm data.

Ionization path length considerations would indicate a larger thruster should start at a lower neutral density. The data of Fig. 4-2 only partially support this viewpoint, but, of course, variables other than chamber diameter are probably also significant. As a simple first approximation to this expected effect of size, the neutral density data of Fig. 4-2 were multiplied by the appropriate chamber diameters and plotted in Fig. 4-3. The shaded area shows the range of starting voltages observed, which should also serve as an estimate for other discharge chambers. Most of the data shown in Fig. 4-3 were obtained in the usual manner with the discharge chamber shell and screen grid connected to cathode potential. The flagged data show the effect of connecting these elements to anode potential. Such a connection is not desirable for normal operation because it would lead to excessive discharge losses. For reducing the required startup voltage, though, such a connection is quite effective. The transition to normal operation can be accomplished by switching from anode potential for the shell and screen grid as soon as roughly 10-100 mA of discharge current is attained.

---

* The accelerator system data were not included in Ref. 1. The screen grid was 0.38 mm thick, had 1.9 mm diameter holes, and 67% open area. The accelerator grid was 0.51 mm thick, had 1.5 mm diameter holes, and 43% open area.
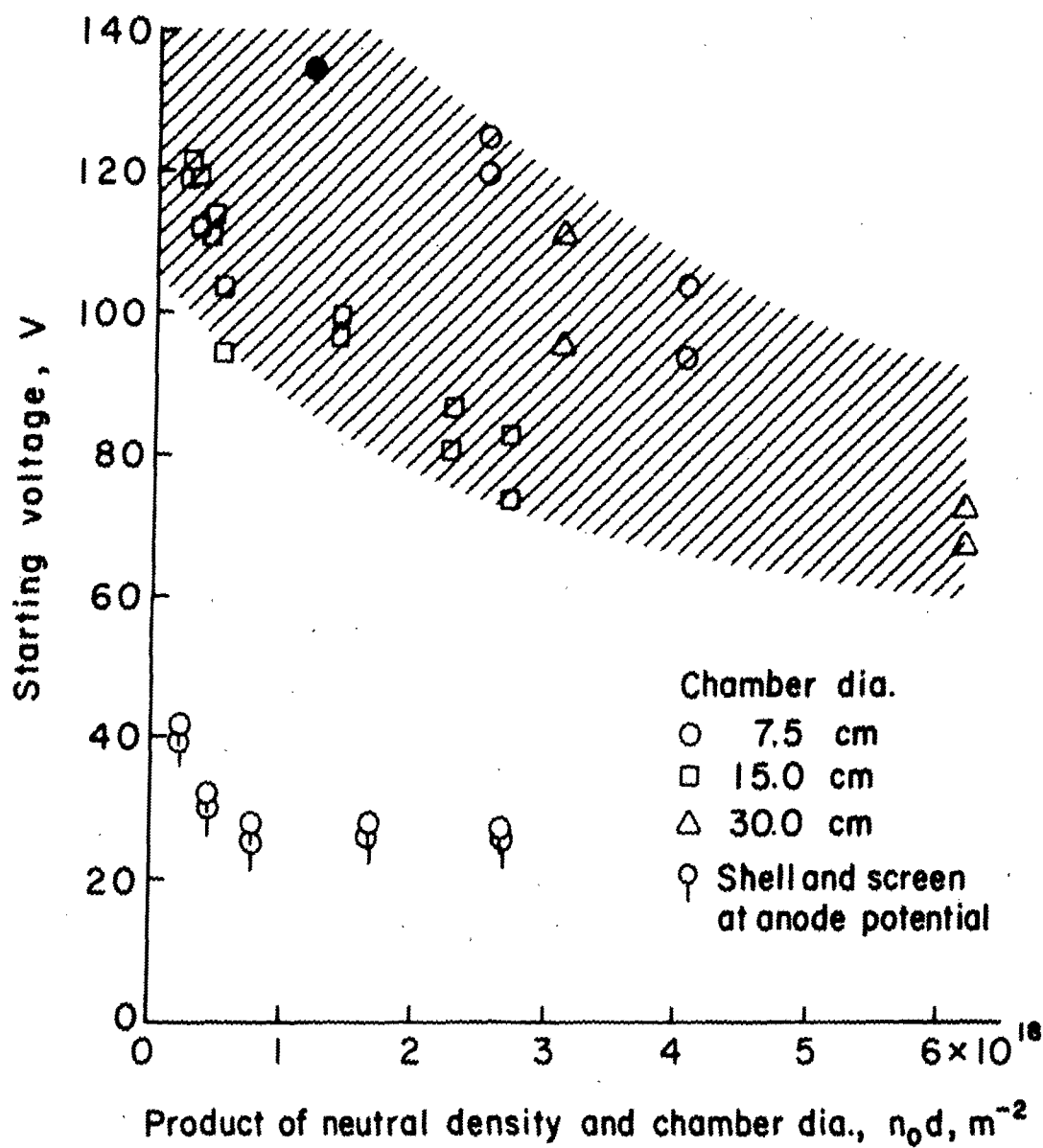
Figure 4-3. Starting voltages as a function of neutral
density times chamber diameter.

V   DISCHARGE CHAMBER PERFORMANCE

by Larry A. Rehn

Operation of multipole discharge chambers with inert gas propellant and refractory metal cathodes has been well documented in previous investigations.[1-4]   The emphasis in this investigation was on the use of a hollow cathode in a multipole chamber.

Apparatus

The multipole discharge chamber used in this investigation is indicated in Fig. 5-1 in its refractory metal cathode configuration.   The discharge-chamber magnet current was about 6 A for all the data reported herein.   This value was found to give near minimum discharge losses and corresponded to an average field integral above the anodes of about 75×10^{-6} Tesla-m (75 Gauss-cm).

The refractory cathode was made from 0.25-mm diameter tungsten. When this cathode was used in the discharge chamber, a similar cathode was used as neutralizer.

The discharge-chamber hollow cathode was a 6.4-mm diameter tantalum tube with an approximately 1-mm thick tungsten tip.   The orifice was 0.79 mm in diameter and a tantalum heat fin was attached to the tip. A similar hollow cathode was used as the neutralizer during the hollow cathode tests, except that the orifice was 0.38 mm in diameter and there was no heat fin.   The neutralizer gas flow was 250 mA-equiv with argon and 50 mA-equiv with xenon.   The neutralizer flows were not included in the discharge performance calculations.
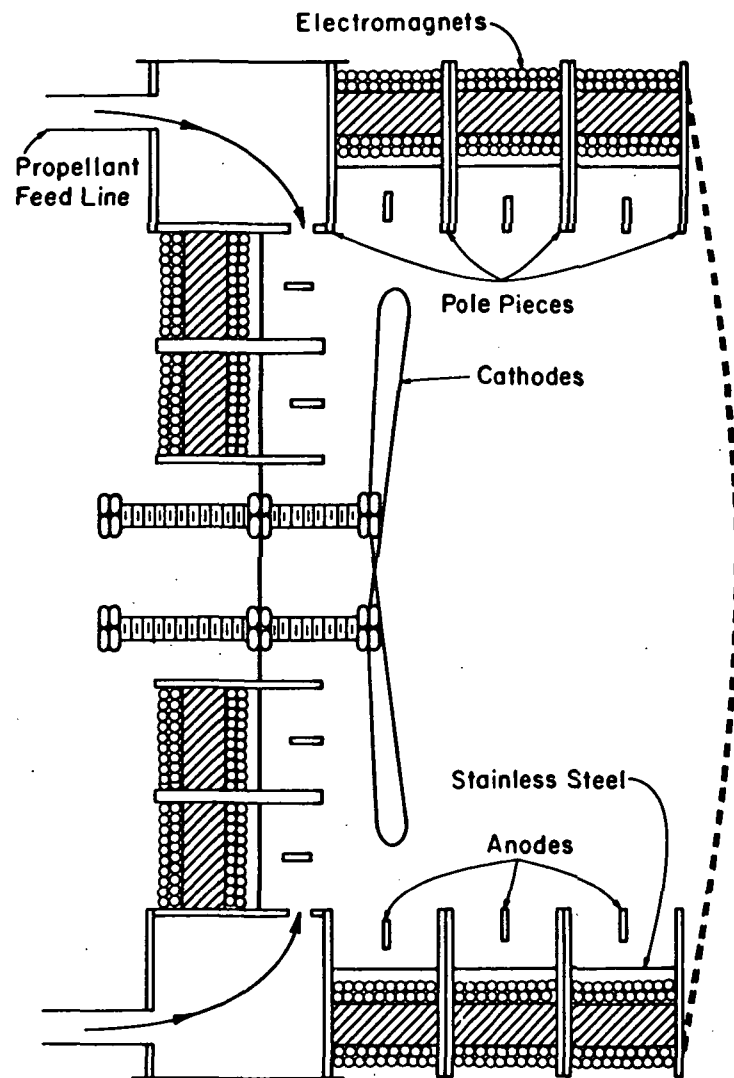
Figure 5-1. Fifteen cm multipole discharge chamber with refractory cathode.

The original pole piece used with the discharge-chamber hollow cathode is shown in the drawings of Fig. 5-2. It was soon discovered, though, that the polyimide insulation (Kapton) on the magnet winding was overheating, with severe outgassing as the result. This problem prompted a change to segmented ceramic insulators. Because the latter insulators were much bulkier than the polyimide, the number of windings was reduced from 20 to 5. The modified assembly (as used for the data presented herein) is shown in Fig. 5-3. The variation of magnetic field strength in the baffle annulus with ampere-turns of field winding is shown in Fig. 5-4. The data in this figure are approximated with a straight line to show that no part of the baffle magnetic circuit was near saturation. The magnetic field strength of the multipole field was found to have little effect on the baffle field.

The accelerator system consisted of dished molybdenum SHAG optics with a 2.2-mm centerline spacing between holes. The open area fractions of the screen and accelerator grids were 0.66 and 0.28. All data presented herein were obtained at +1.0 kV and -0.5 kV.

Refractory Cathode Data

The refractory cathode data were obtained to provide a basis for comparison with hollow cathode data. These data are shown in Fig. 5-5. The curves of Fig. 5-5 are roughly similar to those obtained in earlier investigations with nearly the same configuration. The discharge voltage was held constant at 50 V for all data in Fig. 5-5. Propellant utilizations were corrected for both neutral backflow and double ionization.

36

gap = 0.76 cm

O.D. = 4.7 cm

Outer pole piece

Inner pole piece

(b) Downstream end

Electromagnet windings
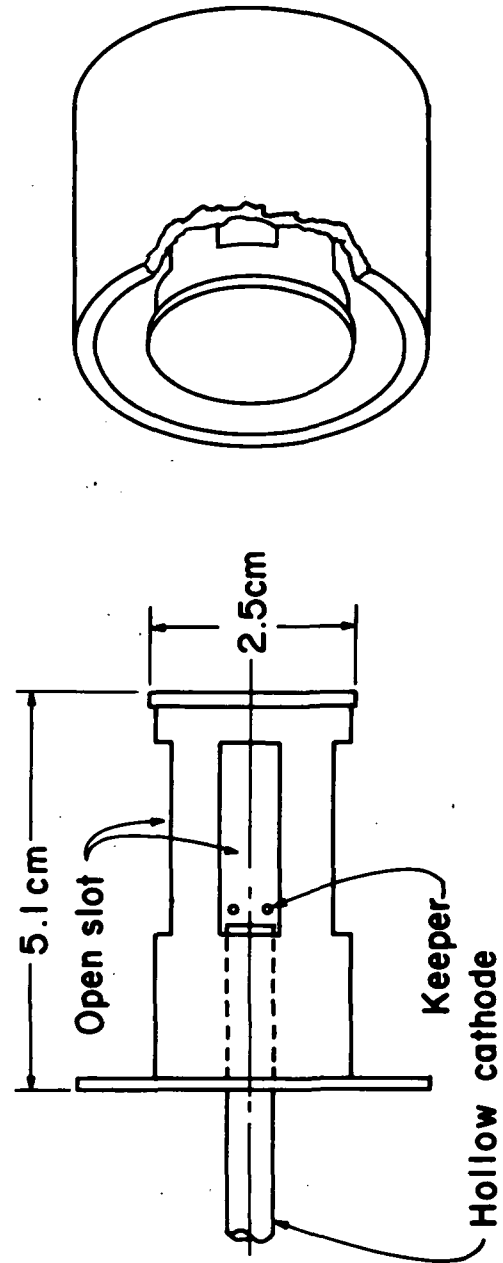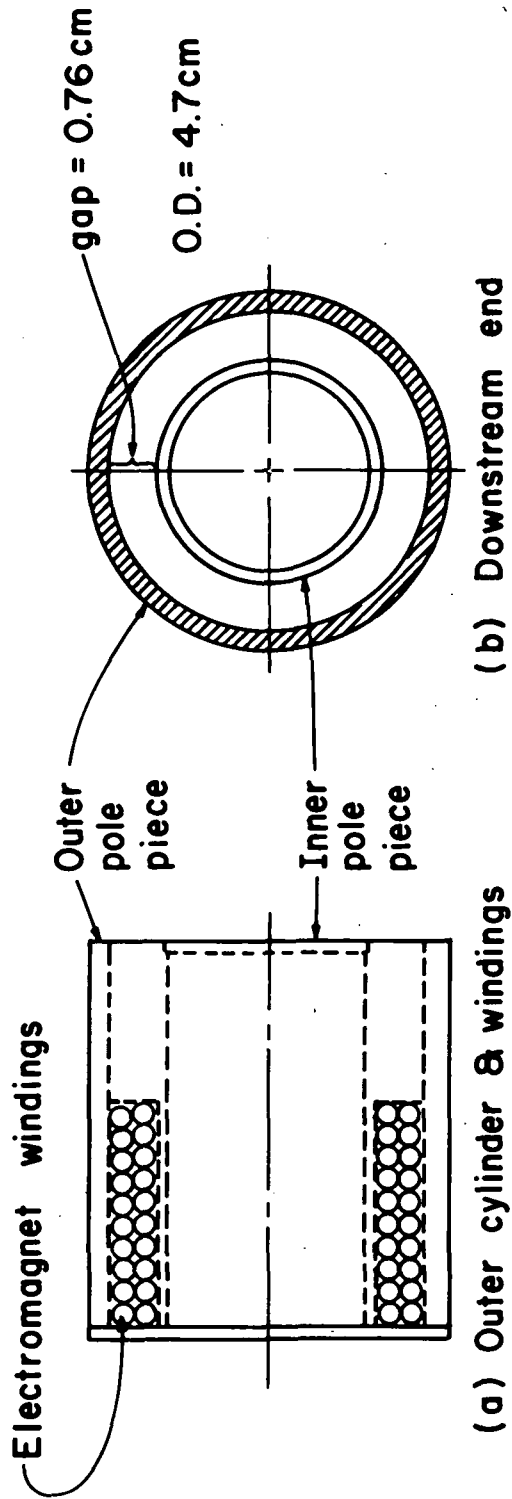
(a) Outer cylinder & windings

2.5 cm

5.1 cm

Open slot

Keeper

Hollow cathode

(c) Inner cylinder & cathode

(d) 3-D View

Figure 5-2. Magnetic baffle used in investigation.

(a) Assembled magnetic baffle
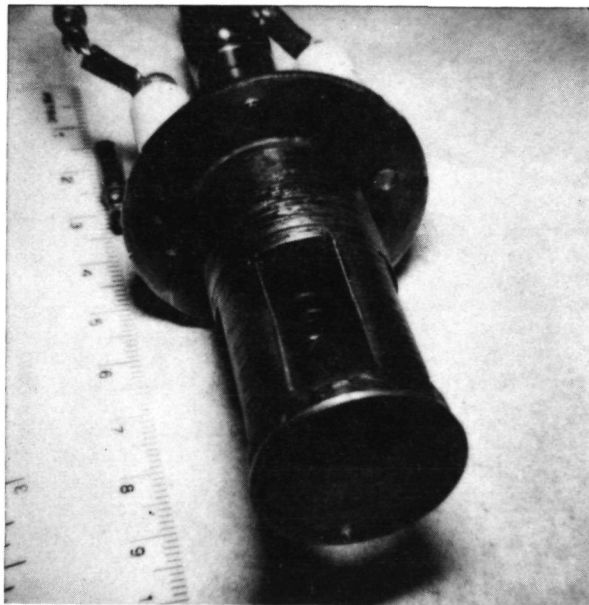
(b) With outer pole piece removed

Fig. 5-3. Photographs of magnetic baffle.
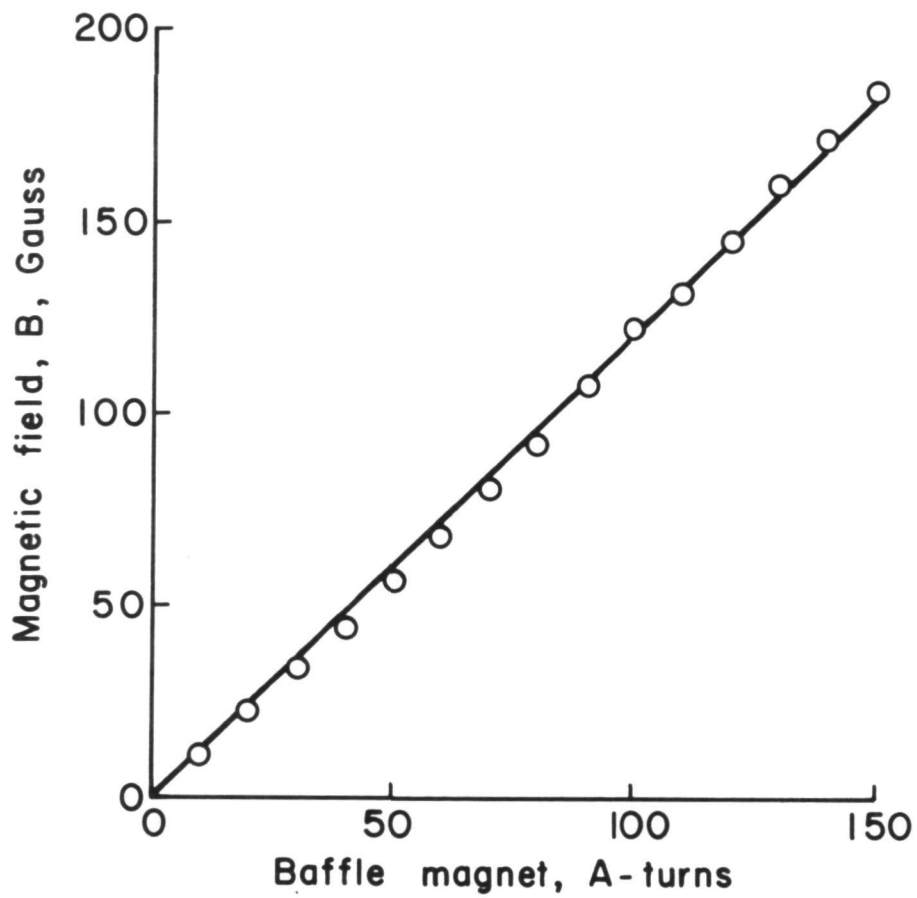
Figure 5-4.   Magnetic field in the baffle annulus
as a function of magnet current.
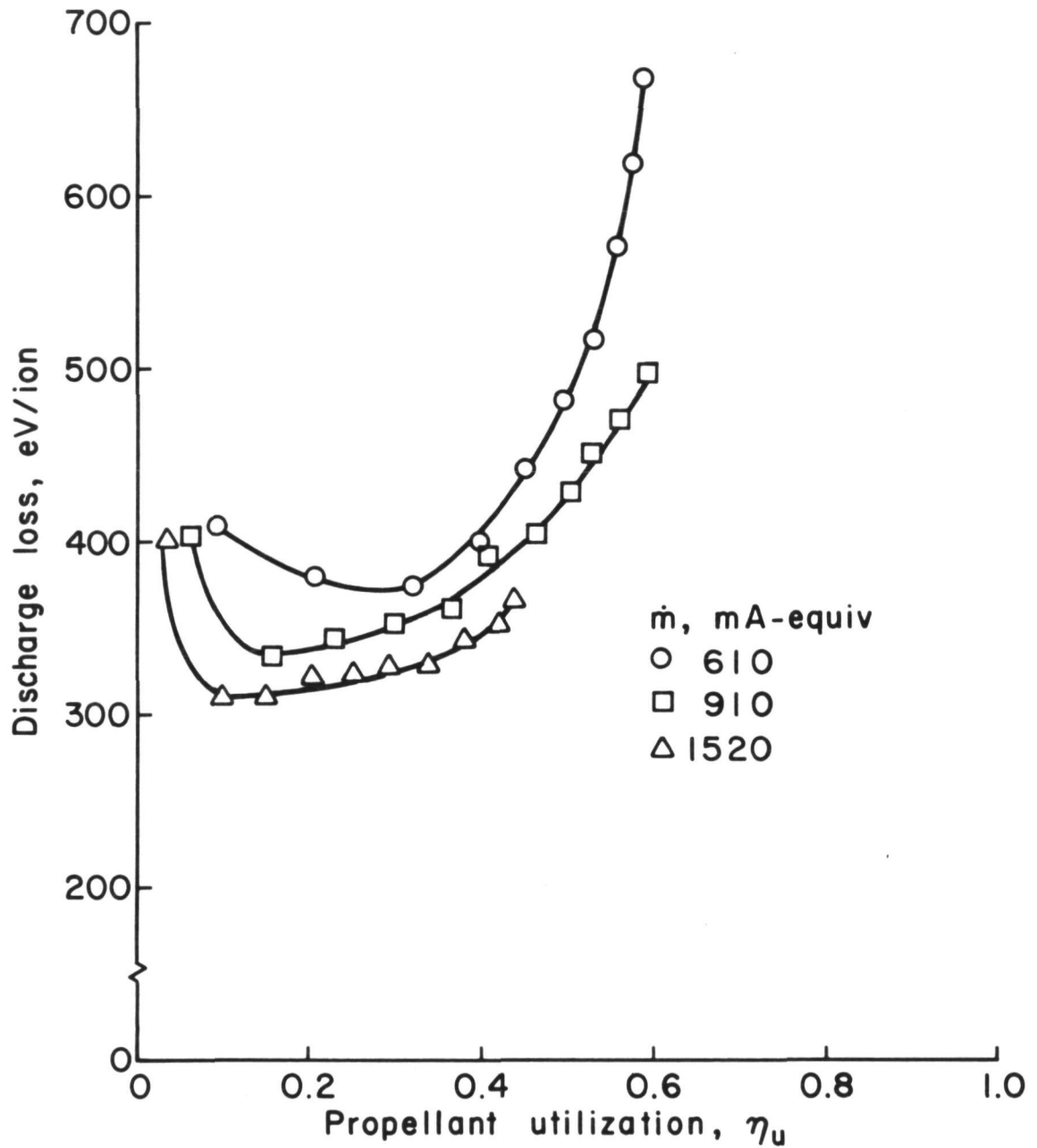
Figure 5-5. Discharge chamber performance of three-section
multipole thruster with argon propellant. Main
and neutralizer cathodes: tungsten wire.

Hollow Cathode Data

Data obtained with the hollow cathode are shown in Figs. 5-6 and 5-7 for argon and xenon propellant. The data shown are corrected for both neutral backflow and double ionization, but do not include heater or keeper powers for the hollow cathode. The keeper power was 3-4 W with argon and 2-4 W with xenon.

The argon hollow cathode data of Fig. 5-6 are similar to the refractory cathode data of Fig. 5-5, except the losses are about 100-200 eV/ion less with the hollow cathode. For the worst case, the keeper power would only account for a small part of this difference. Poor placement of the refractory cathodes (within the fringe magnetic field of the nearest anode) is the suspected cause for most of the difference.

The discharge loss level with xenon was lower than with argon, while the propellant utilization with xenon was greater than with argon. Both of these trends are consistent with previous observations with refractory cathodes.

A typical ion beam profile is shown in Fig. 5-8. All profiles were found to have flatness parameters (average-to-peak current density ratios) between 0.63 and 0.70. The Faraday probe was about 1 cm from the center of the accelerator grid, and farther at the edges. Previous experience with multipole chambers indicates that the flatness parameters would approach 0.9 if extrapolated back to the plane of the accelerator grid.

The ranges of the discharge voltage are shown in Table 5-1 for various propellant flow conditions. The discharge voltage generally decreases for either an increasing total propellant flow rate or an increasing fraction through the main cathode. This is consistent with previous experience with mercury hollow cathodes. The data of Figs. 5-6 and 5-7,
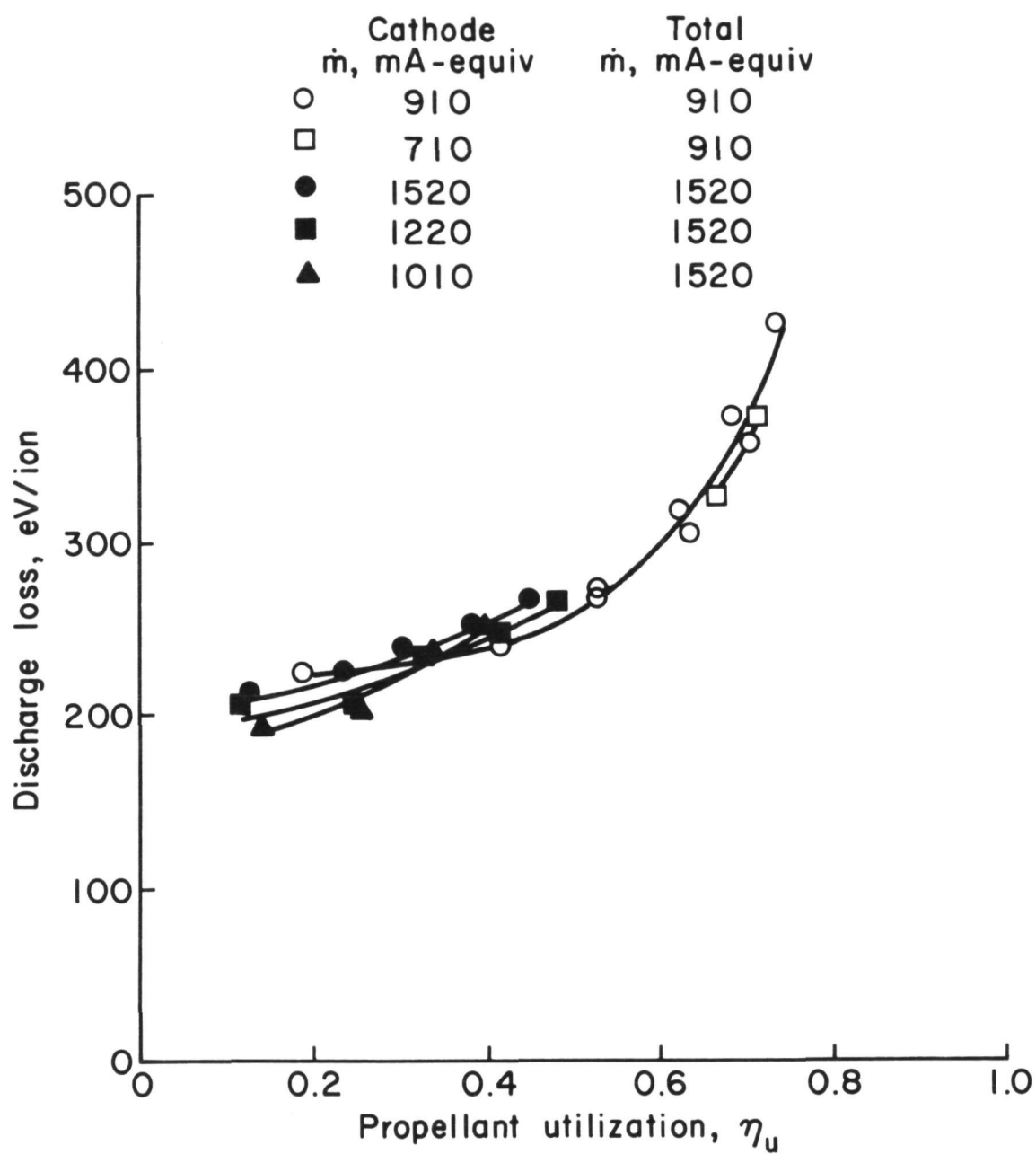
Figure 5-6. Discharge-chamber performance with a hollow cathode. Argon propellant.
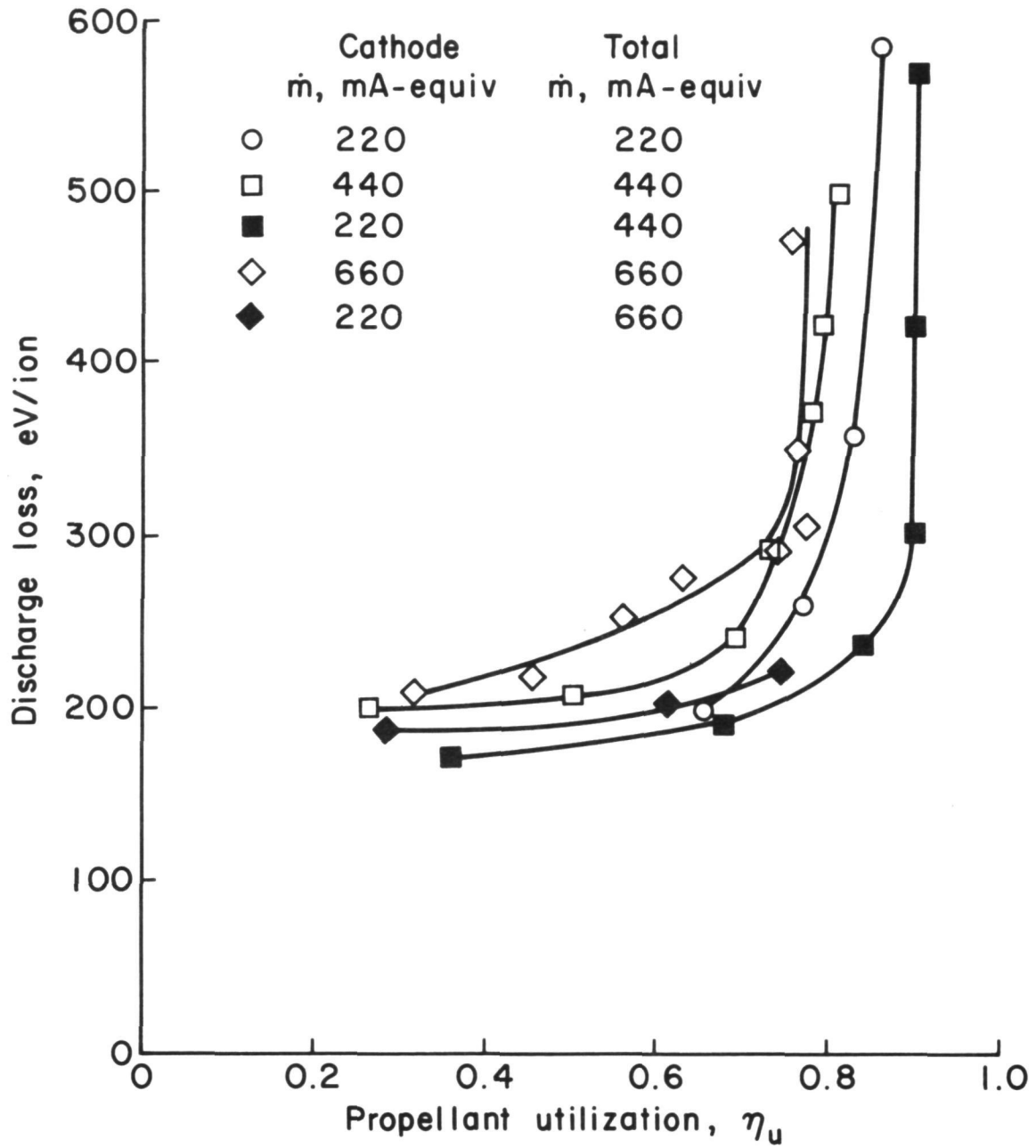
Figure 5-7. Discharge-chamber performance with a hollow cathode. Xenon propellant.
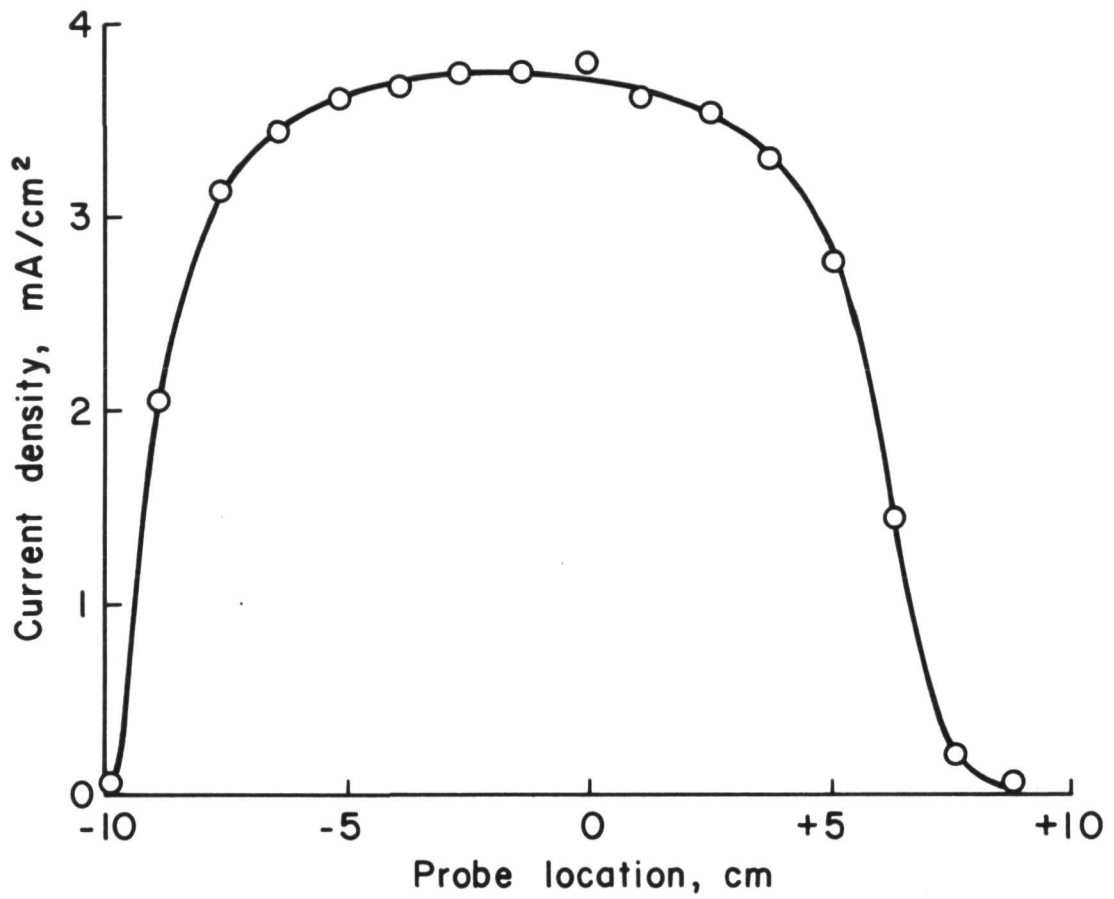
Figure 5-8. Typical ion-beam profile with argon propellant.
(Propellant flow, 1220 mA-equiv.)

TABLE 5-1

DISCHARGE VOLTAGE

(a) Argon

Cathode $\dot{m}_1$ mA-equiv	Total $\dot{m}_1$ mA-equiv	Discharge voltage, V
710	910	51-54
910	910	44-50
1010	1520	40-42
1220	1520	39-41
1520	1520	37-38

(b) Xenon

Cathode $\dot{m}_1$ mA-equiv	Total $\dot{m}_1$ mA-equiv	Discharge voltage, V
220	220	30-54
220	440	28-44
220	660	26-28
440	440	24-40
660	660	23-25

(These voltage ranges are for the data shown in Figs. 5-6 and 5-7.)

as well as Table 5-1, were obtained with little or no baffle magnet
current. This is because this current had little effect on performance,
as shown in Fig. 5-9.* The range shown, though, was limited by power
supply current capability. The discharge-voltage slope shown at 10 A
indicates that larger effects might have been found at higher current
levels.

Tests were also made with a main cathode having a smaller 0.43 mm
orifice. It was anticipated that reducing the orifice size would permit
operation with less flow through the cathode. This, however, was not the
case. Despite the smaller orifice, it was found that the cathode flow
still had to be 1000 mA-equiv, or more, of argon to operate in a reason-
able manner. Even with this high flow, the discharge-chamber performance
with the smaller orifice was poorer than that shown above for the larger
orifice. Changes in the baffle configuration (opening the longitudinal
slots about 50%, then closing them with tantalum foil at either the front
or back) did not significantly improve the poorer performance with the
smaller orifice.

Doubly Charged Ion Production

The production of doubly charged ions was measured at a limited number
of conditions. Some of these conditions are listed in Table 5-2. A sys-
tematic study of doubly charged ion production was made for refractory
cathode multipole chambers.[3] At the same propellant flow, the same dis-
charge current, and the same discharge voltage, the refractory cathode
data of ref. 3 can be compared to the ratio I^{++}/I^{+} for hollow cathode
cathode operation. These estimates are listed in the last
column of Table 5-2. Fairly close agreement could be found for the

---

*The shape of the curve in Fig. 5-9 suggests that, despite precautions,
the baffle current was reversed from the proper direction.
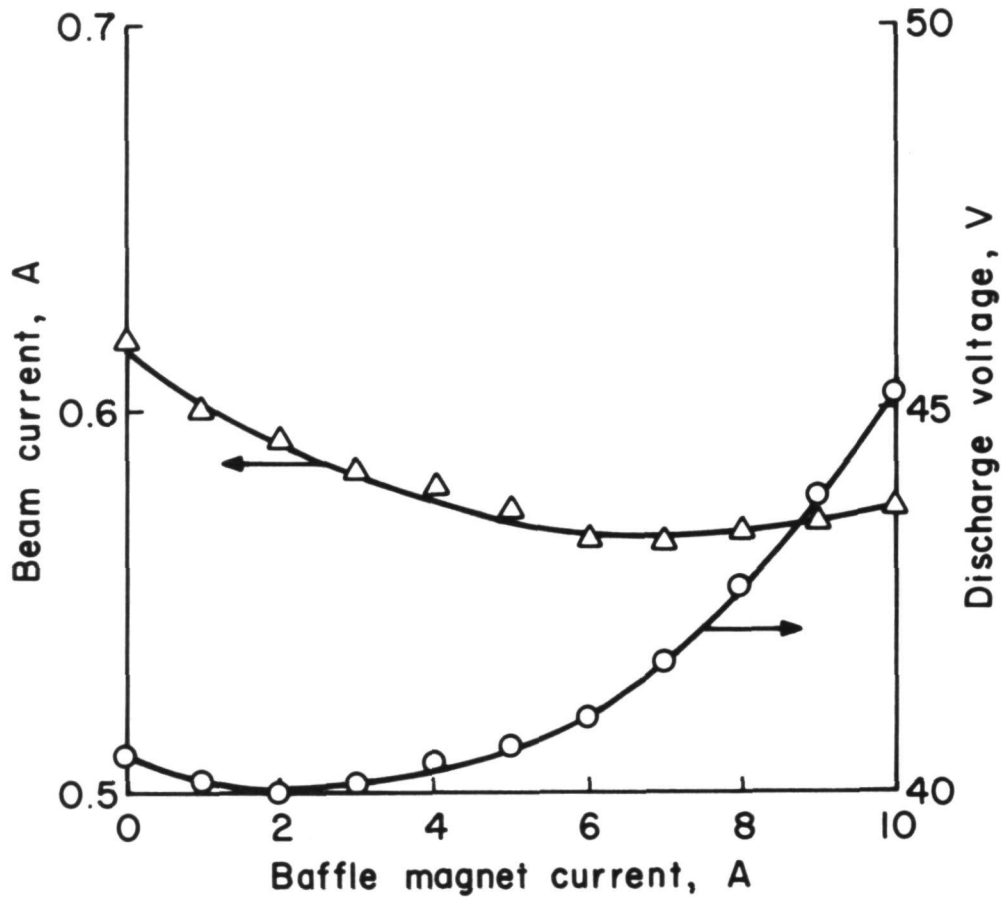
Figure 5-9. Effect of baffle magnet current on beam current and discharge voltage. (Propellant flow, 1217 mA-equiv of argon, all through the cathode. Discharge current, 4A.)

TABLE 5-2

DOUBLY CHARGED ION PRODUCTION

(a) Argon

Total m_1 mA-equiv	J_{Dis}, A	V_{Dis}, V	I^{++}/I^+, Hollow cath.	I^{++}/I^+, Refract. cath.
910	5.	48.	0.052	0.046
1520	4.	39.	0.011	~0.02

(b) Xenon

Total m_1 mA-equiv	J_{Dis}, A	V_{Dis}, V	I^{++}/I^+, Hollow cath.	I^{++}/I^+ Refract. cath.
220	1.5	31.	0.061	~0.06*
440	5.5	28.	0.038	≤ 0.1 *
440	3.	29.	0.018	< 0.1 *
660	6.	25.	0.019	----

*Large extrapolation required in discharge voltage.

argon data operating conditions and the agreement between measured and estimated doubly charged ion production is as good as could be expected. The xenon hollow cathode data were at considerably lower discharge voltages than the refractory cathode data. As a result, the estimate becomes more approximate. The comparison of Table 5-2 shows sufficient agreement for a tentative conclusion: The production of doubly charged ions is the same for both hollow and refractory cathode multipole chambers when operating conditions are otherwise the same. This conclusion is also consistent with the theory of doubly charged ion production.* Except as the plasma uniformity is affected, the production of doubly charged ions should be independent of cathode type. And the plasmas with both cathode types should be quite uniform, as indicated by the beam profiles obtained.

The MESC Effect

The magneto-electrostatic containment effect has been described in connection with the multipole discharge chamber of Moore[5] and Ramsey.[6] Briefly, by operating with the multipole anodes more positive than the bulk of the discharge chamber plasma, the ion losses to the walls of the chamber should be reduced by electrostatic containment. Such biased anode operation was tried and reported in Section III of this report, with no favorable effects observed. It is possible, as mentioned in that section, that possible benefits were obscured by disconnecting some of the anodes. It is clear, though, that biased anode operation results in poor stability with respect to disturbances. Also, without some means of changing the anode-to-discharge current ratio (K_{ab} in Eq. (3-21)), a proper bias will be obtained only over a restricted operating range.

---

*This is the theory of P. J. Wilbur, pp. 46-64 of Ref. 4.

The use of a plasma anode in some configurations is apparently one means of extending the operating range for a given bias. From previous experience with reduced anode areas in mercury thrusters, however, the area of the plasma anode is probably a compromise between excessive discharge losses and the durability of the plasma anode. Another approach to extending the operating range with biased anode operation should also be considered. This approach requires an additional cathode at roughly the desired plasma potential. The combined emission of the conventional discharge-chamber cathode and the plasma cathode is selected to exceed the current capacity for the multipole chamber used. On the other hand, the emission of the conventional cathode alone should never exceed this current capacity. The plasma potential in the discharge chamber should rapidly reach the value where the emission of the plasma cathode is consistent with the current capacity of the discharge chamber. This potential, of course, establishes the proper bias between the plasma and the anodes. Although this approach should effectively control the plasma potential within the discharge chamber, one would expect the same desirable stability as observed in ion-beam neutralization with a plasma-bridge neutralizer.

VI   HOLLOW CATHODES
by Larry Rehn

A variety of hollow cathode tests have been conducted with inert gases. These tests include a 200 hr endurance test, the study of the effect of anode size, and the comparison of neutralizer and bell-jar performance. As a final subject of this chapter, the effect of ion collisions with neutrals is evaluated in terms of spot and plume modes.

200 Hour Endurance Test

An endurance test was conducted in a bell jar using a 6 cm^2 disc located 7 mm from the orifice. The hollow cathode used was made from a 6.4-mm diameter tantalum tube and had a 1.3-mm-thick thoriated tungsten tip, with the tip electron-beam welded onto the tantalum tube. The inserts were close-fitting porous tungsten cylinders 13-mm long with 2.5-mm holes through the axis. The inserts were impregnated with a mixture of barium and strontium carbonates. The cathodes were wrapped with swaged heater wire for about 1 cm near the tip, and then covered with tantalum foil to reduce the radiation heat loss. The approximate orifice diameter was 0.4 mm and the flow of argon was 300 mA-equiv. No radiation fin was used. The keeper current was 0.2 A, while the discharge current was 1.0 A. The keeper and discharge voltages were 35 - 47 V and 30.5 - 46 V.

The wide voltage ranges given above were due mostly to changes in insert condition. These changes were, in turn, felt to be due to the complete disassemblies required to examine the orifice region under

a scanning electron microscope (SEM). The endurance test was thus felt
to be a test of the tungsten tip and the orifice region rather than the
insert. Insert operation under more realistic conditions would be
expected to be consistent with mercury propellant experience. That is,
with proper operating temperature and no exposure to poisoning elements
or compounds, reasonable lifetimes for thruster applications can be
attained.

A micrograph of the cathode orifice region is shown in Fig. 6-1
after 200 hours of operation. Another micrograph is shown of the orifice
with a tungsten wire for reference in Fig. 6-2. By comparison with the
wire (which was carefully measured) the orifice was found to taper from
0.36 mm at the upstream end to about 0.40 mm at the end of the gradual
taper region near the downstream end. In the last 0.1 mm from the surface
the orifice belled out to about 0.44 mm.

Based on these measurements, two estimates were made of total life-
time: One estimate assumed that the gradual tapered region was the
result of equal parts of diameter reduction at the upstream end and
increase at the downstream end. The associated lifetime would be 1000-
2000 hrs. This approach, however, is probably overly conservative be-
cause closures of orifices have seldom been observed in practice.

The other estimate assumed that all changes from a cylindrical
shape were due to material removal and the rate of material removal would
remain constant until the final shape was reached. This final shape was
assumed to be an extrapolation of the rounding shown in Fig. 6-1 near
the orifice, where the radius of rounding equaled the thickness of the
tungsten tip. The associated lifetime with these assumptions would be

Fig. 6-1. Micrograph of cathode orifice region after 200 hours of operation. (See text for operating conditions.)
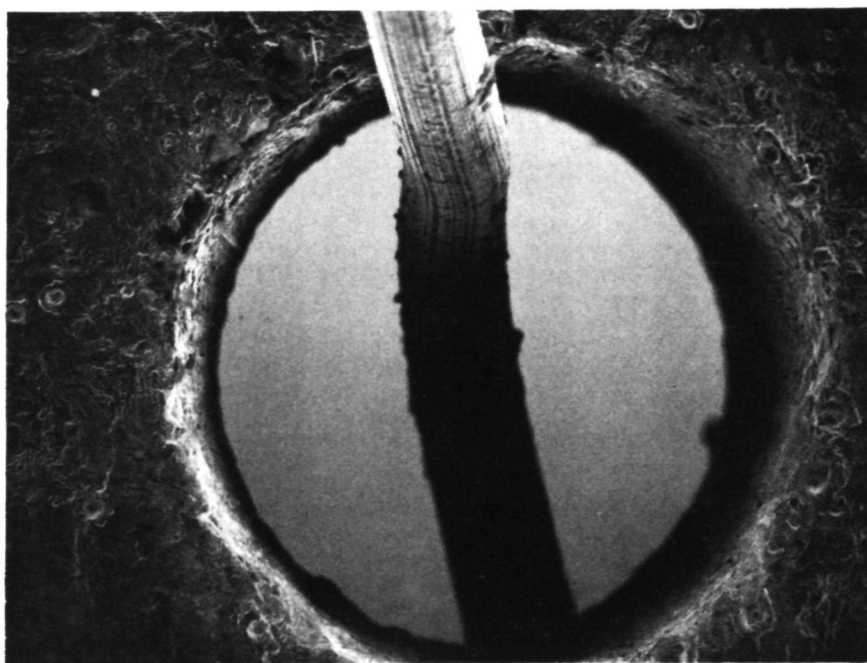
Fig. 6-2. Micrograph of cathode orifice with tungsten calibration wire inserted.

8000-10,000 hrs. This approach is believed to be more representative of the actual wear process.

Two points should be made concerning the 200 hr endurance test and the associated lifetime predictions. The first is that adequate lifetimes appear probable for space applications with inert gas. Although 8000-10,000 hr estimate appears a little short, the operating voltages ($\geq$30 V) were high. Operation at lower voltages should give the needed lifetime increase. As mentioned earlier, the proper insert temperature and no exposure to poisoning elements and compounds should permit any required insert lifetime.

The other point that should be made is that future lifetime estimates using the SEM can be far more accurate than the estimates given herein. Most of the uncertainty herein concerns the initial dimensions. The wire was used for calibration after the entire endurance run was completed. In the future, SEM micrographs with a calibrating wire should be made before operation to establish the initial dimensions.

A final comment on SEM micrographs concerns the surface texture. Micrographs in the last annual report showed localized textures strongly suggestive of melting.[1] The typical texture after 200 hr was a laminar one suggestive of crystal planes (Fig. 6-3(a)). It seems likely that melting takes place only when a chip or edge protrudes into the plasma (the probable cause for the previously observed "melting"), or when a cathode tip is overheated. The two textures described above should not, however, be considered the limit of possible textures. An earlier SEM micrograph of an orifice region after many hours of mercury propellant operation showed a large number of very small (compared to the orifice)

54
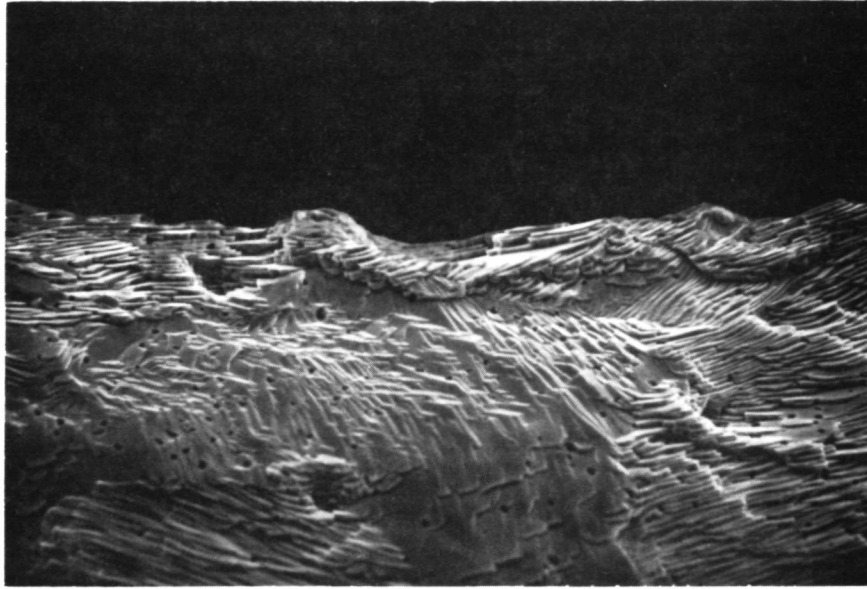
(a) Crystal planes (1200x)
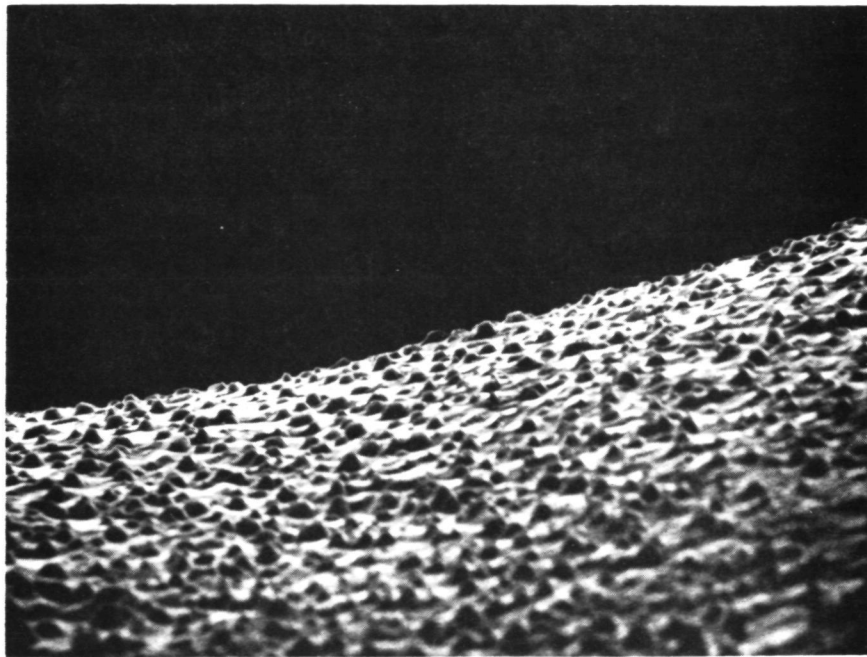
(b) Mounds (700x)

Fig. 6-3. Micrographs showing surface textures near orifice.

rounded or pointed mounds (Fig. 6-3(b)). These mounds were distributed on an otherwise much smoother surface.

Bell Jar Simulation and Anode Size

Selection of anode size and anode-cathode distance both present problems when simulating inert-gas main cathode or neutralizer performance in a bell jar. Experimentally, the coupling voltage increases with increasing anode-cathode distance. This observation is consistent with previous mercury hollow cathode experience. The anode size effect, though, is not as consistent. No significant anode size effect for anodes about 2.5 cm in diameter, or larger, has been reported in mercury hollow cathode literature. Using inert gases, with other parameters held constant, the coupling voltage decreases with increasing anode size. The cylindrical anode shown in Fig. 6-4 was the largest used in the investigation herein and appeared to give operation closest to that observed with a neutralizer. This cathode size effect, though not consistent with mercury experience, is similar to an anode effect observed by Cobine in plasma experiments.[2] Cobine found that a small anode performs in a manner similar to a probe that collects random electron current. If the electron current demanded by the external circuit exceeds that collected by the physical area of the anode, then a reversed sheath (anode more positive than the plasma) will surround the anode and effectively increase the anode size. This reversed sheath, of course, also increases the total cathode-anode coupling voltage.

The adsorption of mercury can occur on a surface below 300°C,[3] while no similar adsorption of inert gases can occur near operating temperatures.[4] The possible adsorption of mercury on the anode surface could
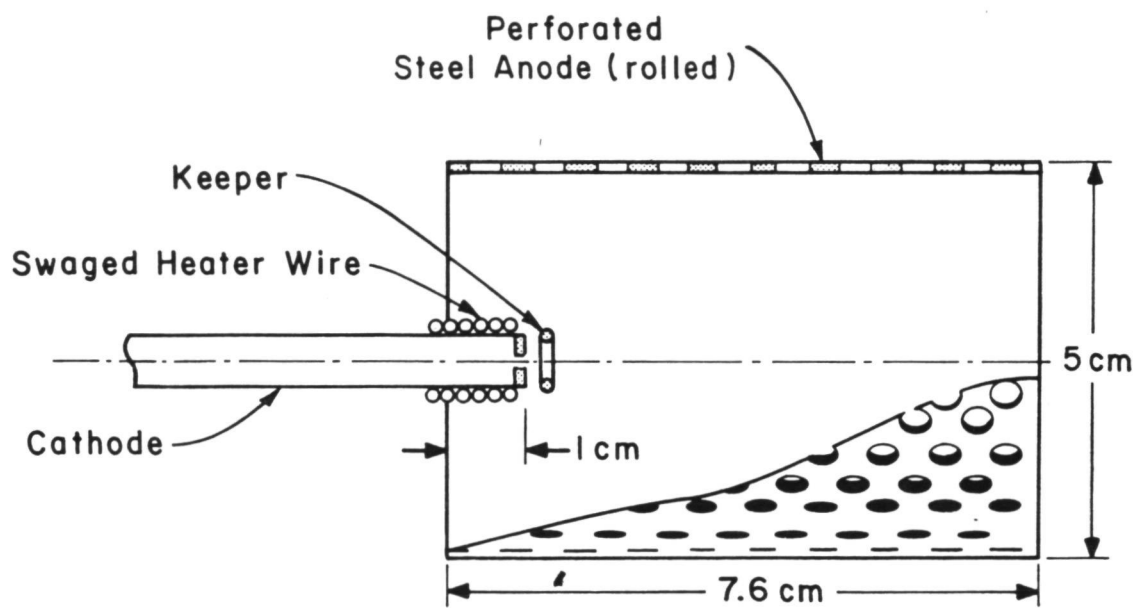
Figure 6-4. Bell-jar test configuration with large anode.

possibly offset any effects of small anode size when using that propellant. Regardless of the explanation, however, tests to date clearly indicate more of an anode size effect with inert gases.

Comparison of Neutralizer and Bell Jar Operation

Data are shown in Fig. 6-5 for both neutralizer and bell-jar operation, with the latter obtained using the anode shown in Fig. 6-4. While comparisons were not always consistent, Fig. 6-5 shows the usual case of higher coupling voltages for bell-jar operation. Also shown in Fig. 6-5 is the usual higher voltage operation with low flow rates and/or light gases. Although the terminology is less clear with inert gases, we follow mercury cathode experience and call the higher voltage operation the "plume" mode and the lower voltage operation the "spot" mode.

Most of the difference between neutralizer and bell-jar data in Fig. 6-5 can be attributed to the two methods of measuring coupling voltage. We have discussed the bell-jar operation earlier in this chapter, and expect the anode to be within several volts of plasma potential in the plume region when a large anode (Fig. 6-4) is used. For neutralizer operation, though, the coupling voltage is measured between the cathode and the vacuum facility. Because the ion beam is positive relative to the vacuum facility, the coupling voltage between cathode and plasma is actually greater than that shown in Fig. 6-5. The potential of the ion beam relative to the vacuum facility is shown for a survey 5 cm downstream of the accelerator in Fig. 6-6(a), together with the electron temperature in the same plane in Fig. 6-6(b). The survey of Fig. 6-6 corresponds to only one operating point in Fig. 6-5, but it appears significant that the average plasma potential in the beam is approximately equal to the

58
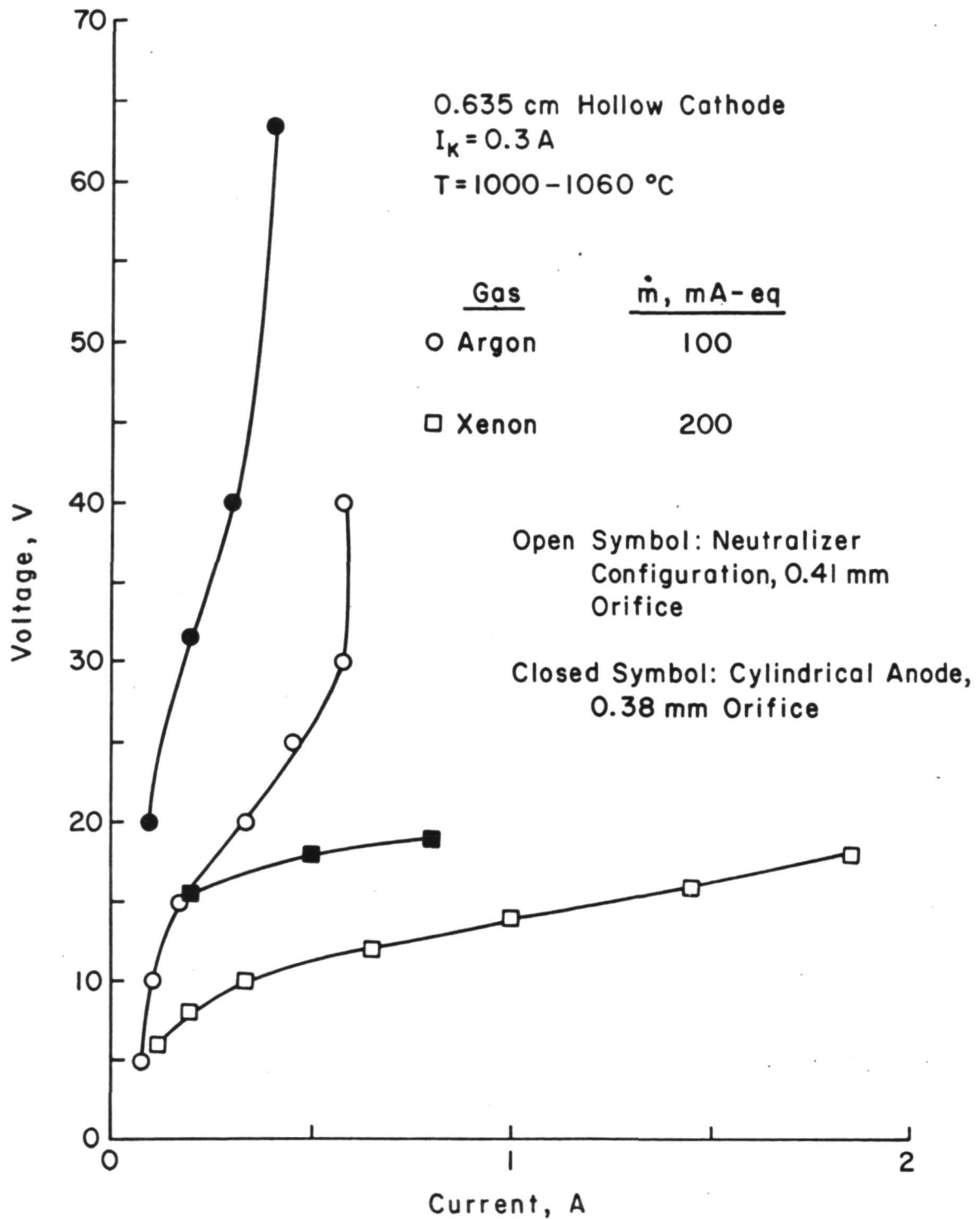
Figure 6-5. Comparison of bell-jar and neutralizer hollow-cathode data.

59
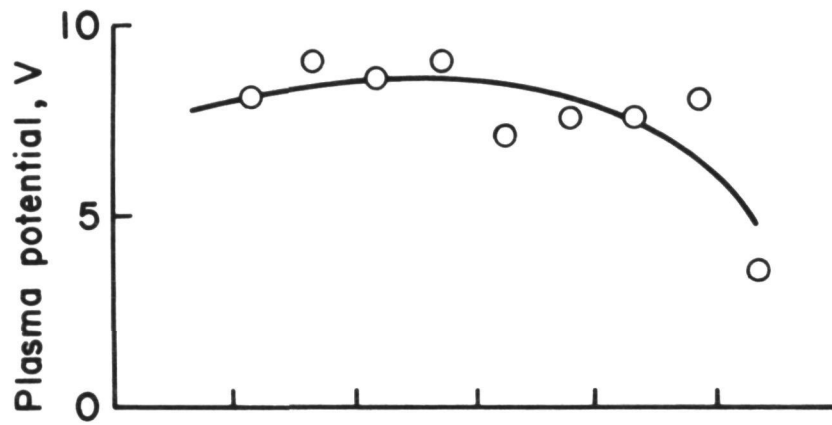
(a) Plasma potential survey.
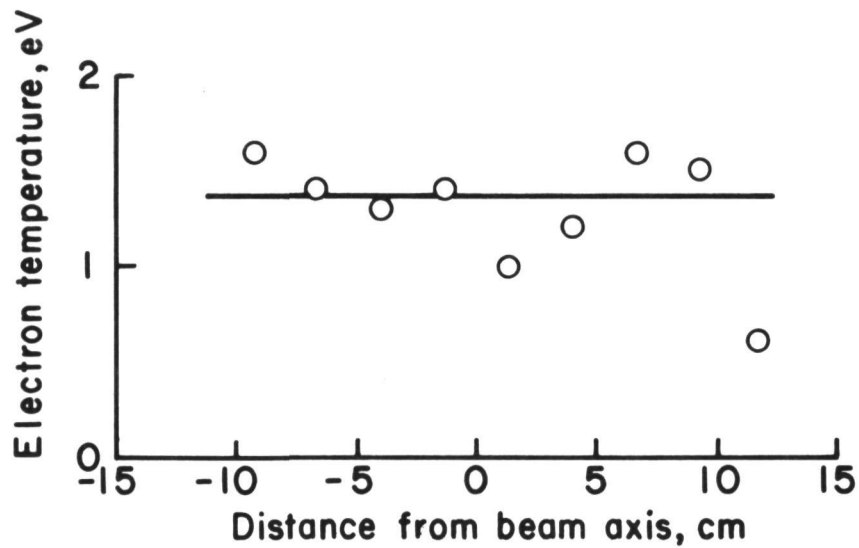
(b) Electron temperature survey.

Figure 6-6. Beam survey during neutralizer operation. Neutralizer orifice, 0.34 mm; mass flow, 200 mA-equiv of argon. Keeper operation, 0.3 A and 16 V. Neutralizer coupling, 0.5 A and 11 V.
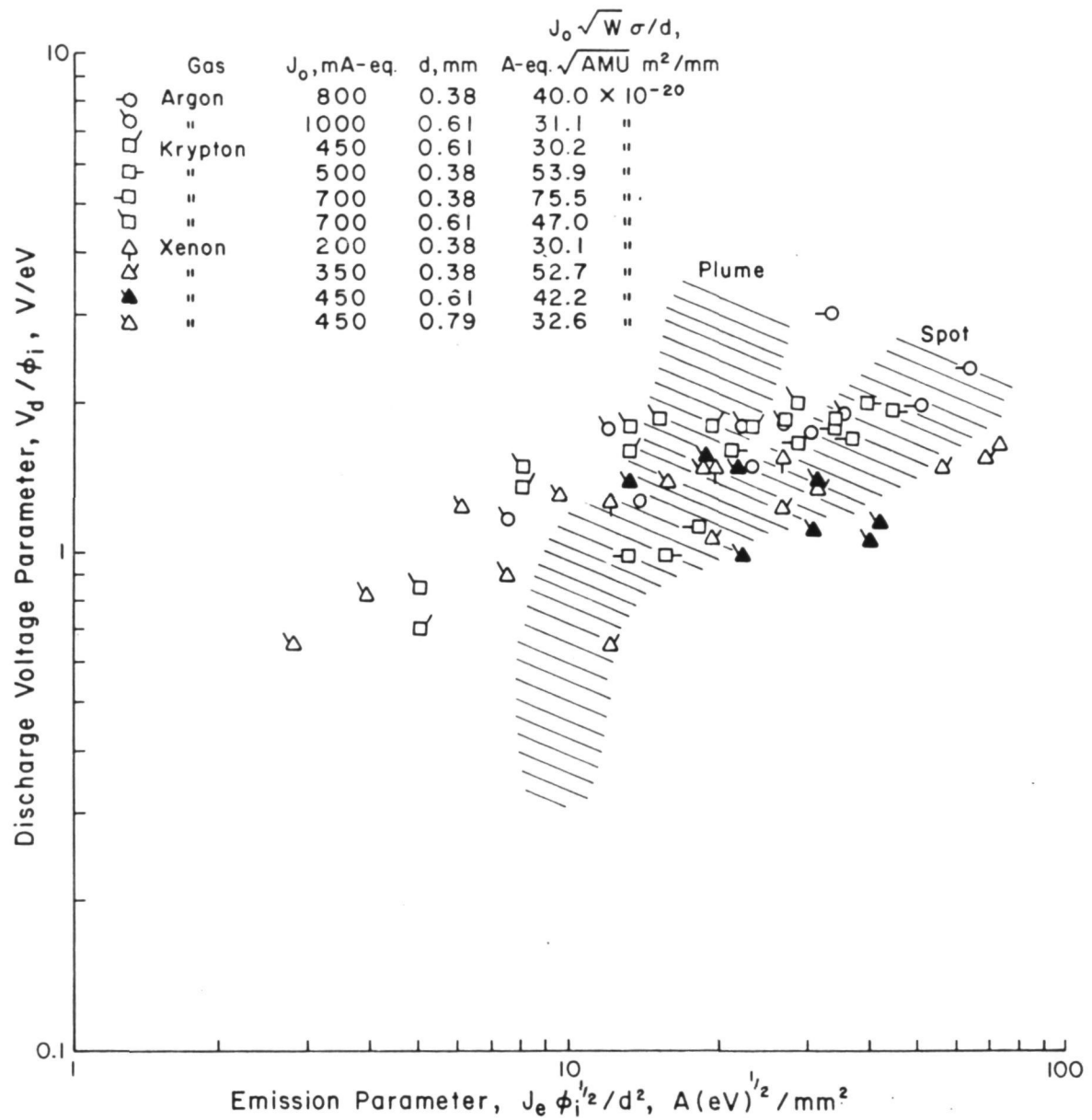
Figure 6-7. Comparison of bell-jar and neutralizer hollow-cathode data. Bell-jar data shown by symbols, neutralizer data by cross-hatched region.

0.635 cm Conventional Hollow Cathode

0.61mm Orifice; Heat Radiation Fin

Bell Jar; Cylindrical Anode

Xenon

$I_K = 0.3$ A; $21V \leq V_K \leq 24V$

$T = 1000 \, ^\circ C$

$\dot{m} = 450$ mA-equivalent

$p = 8 \times 10^{-4}$ torr (Actual Pressure)

O   Visual "Spot" Mode

□   Visual "Plume" Mode
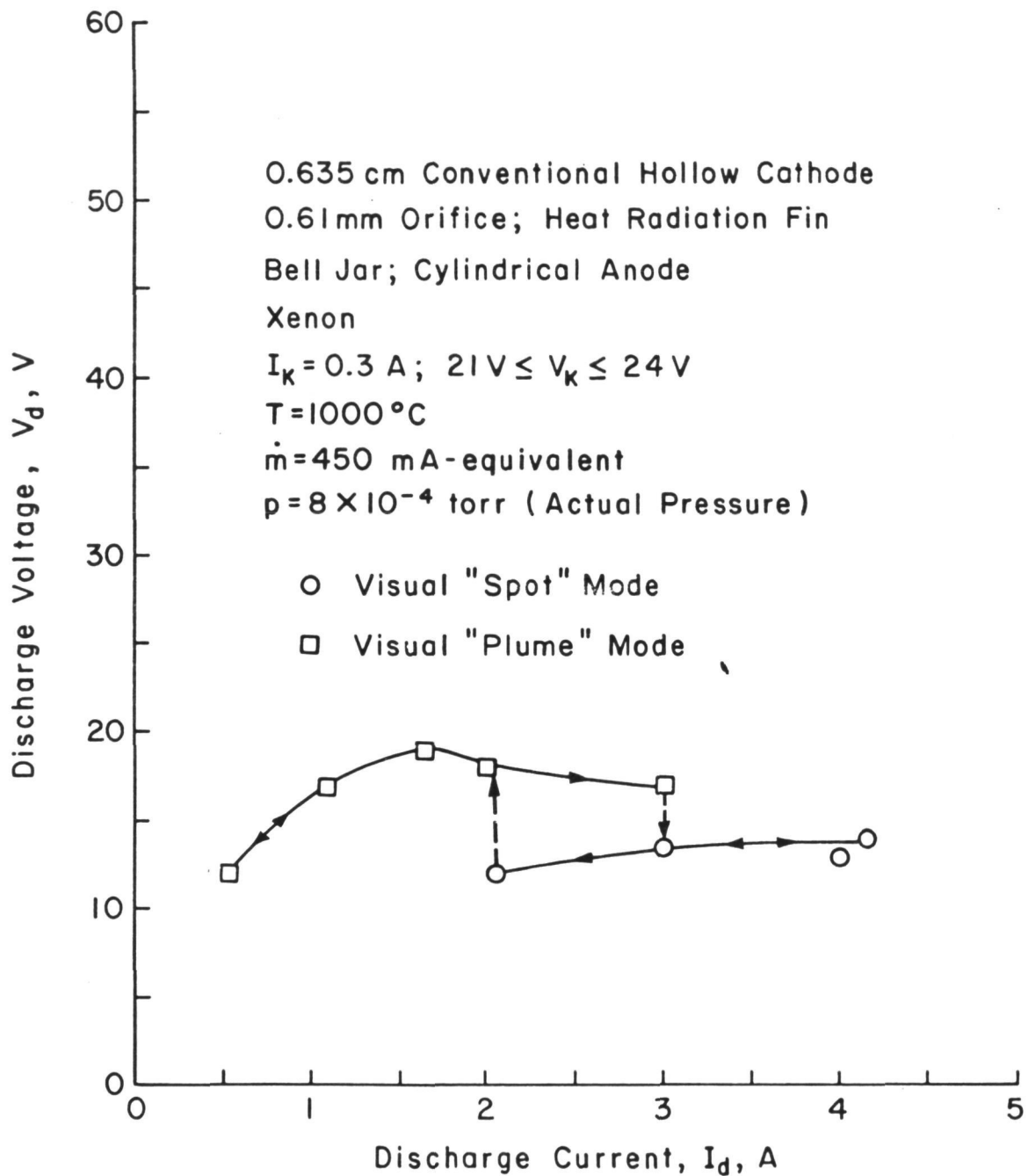
Figure 6-8.   Xenon hollow-cathode data with transition between
spot and plume modes.

difference between neutralizer and bell-jar data at that operating
point. Until more definitive data become available, the anode in
Fig. 6-4 should be assumed to give close to plasma-anode operation.

Bell-jar data obtained with the anode of Fig. 6-4 are also shown
in Fig. 6-7, using the correlation parameters developed in the preceding
annual report.[1] The cross-hatched area of Fig. 6-7 indicates the range
of neutralizer data with the upper branch to the right associated with
the plume mode and the lower branch to the right associated with the
spot mode. There is a larger spread in the bell-jar data, particularly
in the direction of lower values of the emission parameter. There are
also, however, a large number of data that fall in, and close to, the
neutralizer spot mode branch. This latter distribution seems reasonable
inasmuch as all the bell-jar data shown in Fig. 6-7 are for flow parameter
values ($J_0 \sqrt{w} \sigma/d$) of $\geq 30 \times 10^{-20}$, which corresponded to the spot mode
branch in the neutralizer data.

<div align="center">Xenon Spot Mode Operation</div>

In general, the low-voltage, high-current "spot" mode data with
inert gas still showed significant plume luminosity when operated in
a bell jar. In fact, the plume was always visible with anodes smaller
than that shown in Fig. 6-4. With the larger anode, though, operation
with xenon resulted in a spot mode in which no plume luminosity was
evident relative to the brilliance of the spot in the orifice. It is
probably significant that the transition to the spot mode was discon-
tinuous and cycling between plume and spot modes involved a hysteresis
loop (shown in Fig. 6-8). The discontinuous operation and hysteresis
loop are both fairly typical for mercury propellant.

The spot mode has since been observed several times with the anode shown and xenon propellant. No equivalent operation has been observed, though, with argon.

Ion Drift in Vicinity of Orifice

The electric field near the orifice has the direction required to extract electrons. This electric field direction therefore tends to cause ions to drift upstream, back into the hollow cathode. At the same time, the neutral atoms escaping from the cathode would tend to carry along ions by collisions. The hypothesized condition for the spot mode is such that the ions are carried out with the neutrals. If the ions are carried away from the orifice in this manner, then the electron space charge in this region can be neutralized without the production of any additional ions. Conversely, in the plume mode ions would not be carried out with the neutrals because a larger adverse potential difference is assumed to exist. The glow in the plume region would be associated with ion production required in this region. Bistable operation, as shown in Fig. 6-8, is also consistent with this model. In the spot mode a potential difference small enough to permit ions to be carried into the plume region can be stable because no higher voltages will be required. If the potential difference should rise above the value over which ions can be carried, then the ions will have to be produced in the plume region. If the production mechanism requires higher voltages (as might be expected), then the higher voltages would prevent return to the spot mode.

The limiting condition between the two modes is reached when the electric field is just sufficient to keep the ions drifting upstream as rapidly as the neutrals are forcing them downstream. To determine

the ion drift velocity under an electric field E, we do a force balance on an ion,

$$eE = p_i \nu_i \qquad (6\text{-}1)$$

where e is the electronic charge, p_i is the drift momentum of the ion, and ν_i is the collision frequency of the ion. Substituting the product of ion mass and ion drift velocity, $m_i v_d$, for p_i, and solving for E,

$$E = m_i v_d \nu_i/e \ . \qquad (6\text{-}2)$$

For the desired limiting condition, the drift velocity is replaced with the acoustic velocity v_a. With the substitution of

$$\nu_i = 2^{\frac{1}{2}} \pi n_o d_a^2 \overline{v}_o \ , \qquad (6\text{-}3)$$

where d_a is the atomic collision diameter and $\overline{v}_o$ is the most probable atomic velocity $(\overline{v} = (8 kT_o/\pi m)^{\frac{1}{2}})$,[*] together with the substitution of the the acoustic velocity,

$$E = 2^{\frac{1}{2}} \pi n_o d_a^2 m_i v_a \overline{v}_o/e \ . \qquad (6\text{-}4)$$

The integral of Edx gives the total adverse potential difference over which ions can be carried.

$$\Delta V = (2^{\frac{1}{2}} \pi d_a^2 m_i v_a \overline{v}_o/e) \int n_o \ dx \qquad (6\text{-}5)$$

The flow in a hollow cathode orifice is normally in the slip-flow regime. For the flow downstream of the orifice, n_o will be approximated with

---

[*]Ions are assumed to have the same random velocity distribution as the neutrals. For lack of better information, the cross section for an ion-neutral collision is assumed the same as for a neutral-neutral collision.

free molecular flow theory. Using $n_{o, ref}$ as the equivalent source pressure just upstream of the orifice exit, the integral $\int n_o \, dx$ on the orifice axis can be replaced by $n_{o, ref} \, d/2$, where d is the orifice diameter. (The equivalent source pressure is the value required to give the same flow through a thin-plate orifice of diameter d.)

$$\Delta V = \pi \, d_a^2 \, d \, m_i \, n_{o, ref} \, v_a \, \bar{v}_o / 2^{\frac{1}{2}} \, e \qquad (6-6)$$

The relationship between $n_{o, ref}$ and the equivalent current of neutral flow is

$$J_o = e \, n_{o, ref} \, \bar{v}_o \, A/4 = \pi \, e \, n_{o, ref} \, \bar{v}_o \, d^2/16 , \qquad (6-7)$$

which can be substituted into Eq. (6-6) to give

$$\Delta V = 2^{7/2} \, d_a^2 \, m_i \, v_a \, J_o / d \, e^2 . \qquad (6-8)$$

Inasmuch as most hollow cathodes are operated over a narrow temperature range, a mean value of 1000°C will be assumed. Substituting for the various constants, Eq. (6-9) can be rewritten as

$$\Delta V = 3.1 \times 10^{15} \, d_a^2 \, J_o \, W^{\frac{1}{2}}/d , \qquad (6-9)$$

where W is the atomic weight of the propellant. Among the major limitations to the accuracy of this calculation are: (1) The neutral temperature was assumed equal to tip temperature, while it is probably higher than this value; (2) the atomic collision diameter is smaller at the tip temperature than near 0°C, but data are generally limited to temperatures near the latter value; (3) the ion-neutral collision diameter is probably smaller than the neutral-neutral collision diameter, but only the latter is generally available; and (4) due to the slip-flow regime,

there are probably Maxwellian-tail ions that are knocked into the plume region at higher values of ΔV than given by Eq. (6-9). In sum, Eq. (6-9) can only be considered a rough indication of the permissible adverse potential difference for transition between spot and plume modes.

Values from Eq. (6-9) can be compared to experimental results. The atomic collision diameters for Ar , Xe , and Hg are 3.7, 4.9, and 6.3 x 10^{-10} m (0°C).[5] With these substitutions, Eq. (6-9) becomes

$$\Delta V = 2.7 \times 10^{-3} J_0/d \quad (Ar) \qquad (6-10)$$

$$\Delta V = 8.5 \times 10^{-3} J_0/d \quad (Xe) \qquad (6-11)$$

$$\Delta V = 17.4 \times 10^{-3} J_0/d \quad (Hg) \qquad (6-12)$$

The most complete probing of plasma conditions in and around a hollow cathode was conducted with mercury propellant.[6] With a 0.75 mm orifice and a 0.15 A-equiv flow, an experimental potential increase of 3-4 V was found downstream of the orifice when operating in the spot mode, while the increase was higher (6-8 V) in the plume mode. For the same conditions, Eq. (6-12) gives 3.5 V.

Some probe measurements were made of the plume plasma with xenon propellant. Although not as detailed as those obtained with mercury propellant, they also indicated that the variation downstream of the orifice did not exceed a few volts when operating in the spot mode. For the conditions shown in Fig. (6-8), Eq. (6-11) gives 6.3 V.

A more general case may also be of interest. The transition to spot mode for a number of tests with mercury propellant was found to occur at flows of 0.27 ± 0.13 A-equiv per mm of orifice diameter.[7] From Eq. (6-12), this flow range corresponds to 2.4 - 7.0 V.

The calculations thus indicate that ions can be carried along by the neutrals against adverse potential differences of the order of those observed downstream of the orifice during spot mode operation. The hypothesized mechanism for ions reaching the darkened plume region in the spot mode therefore appears realistic.

A scaling expression based on this theory should also be of interest. From Eq. (6-9), the ΔV is proportional to $J_o W^{\frac{1}{2}} \sigma / d$. Except for the use of a momentum cross section instead of an ionization cross section, this expression is the same as the performance-correlation flow parameter derived in the previous annual report. The two cross sections are roughly proportional to each other, so that the two expressions should organize data in a similar manner. A more serious matter might be the inclusion of an ionization potential ϕ_i. A ΔV should be divided by ϕ_i to (ignoring a constant electronic charge) nondimensionalize it. The ionization potential, though, covers a fairly small range compared to the other parameters, so that this inclusion is not critical.

VII GAS FLOW CONTROL

by Donald C. Trock

An electronic control circuit has been designed and constructed to demonstrate the practicality of a gas flow control incorporating components suitable for later development into a flight-type system. Inasmuch as electromechanical devices have had a poorer reliability record in space than electrical or electronic devices without mechanical motion, the minimization or elimination of such motion was the primary criterion used in the selection of flow control components.

Measurement of gas flow uses a thermocouple type flowmeter (Hastings Linear Mass Flowmeter, 0-10 sccm model[1]). A panel meter provides a direct readout in standard cubic centimeters per minute (sccm), although a conversion factor is normally required for gases other than air. Terminals on the back of the flowmeter control unit provide a linear voltage of 0-5 Vdc, corresponding to 0-100 percent of full scale. Full scale was 10 sccm for the flowmeter used in the control described herein, although other models of this type of flowmeter could have been used and are available in maximum flows up to 50,000 sccm. With no moving parts involved, this general type of flowmeter was felt to be well suited to spaceflight applications.

Gas flow is controlled by a piezoelectric valve (Veeco Piezoelectric Valve, Model PV-10,[2] see Fig. 7-1 for photographs, Fig. 7-2 for schematic representation). This valve contains a piezoelectric crystal, 3.5 cm in diameter and 1 mm thick. A small resilient pad (Viton) is glued to the bottom of the crystal and is lightly preloaded against the exit orifice
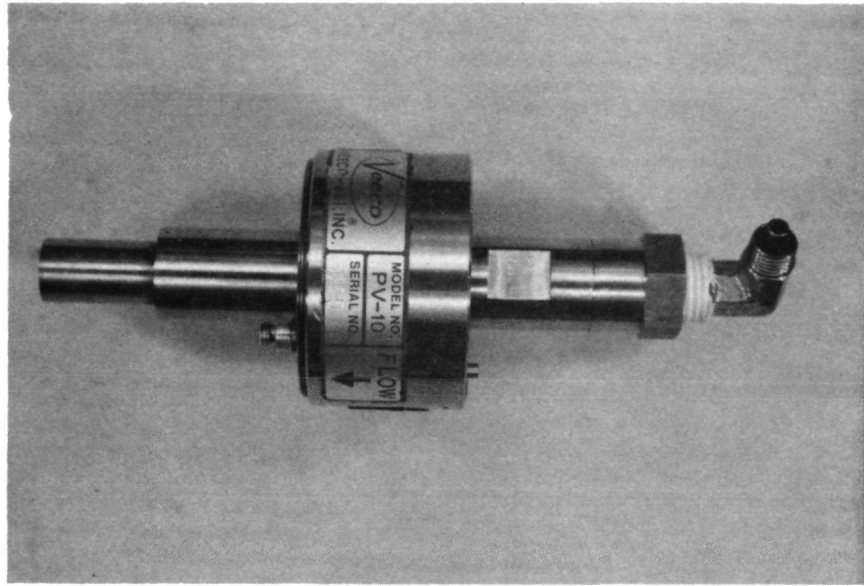
(a) Assembled valve
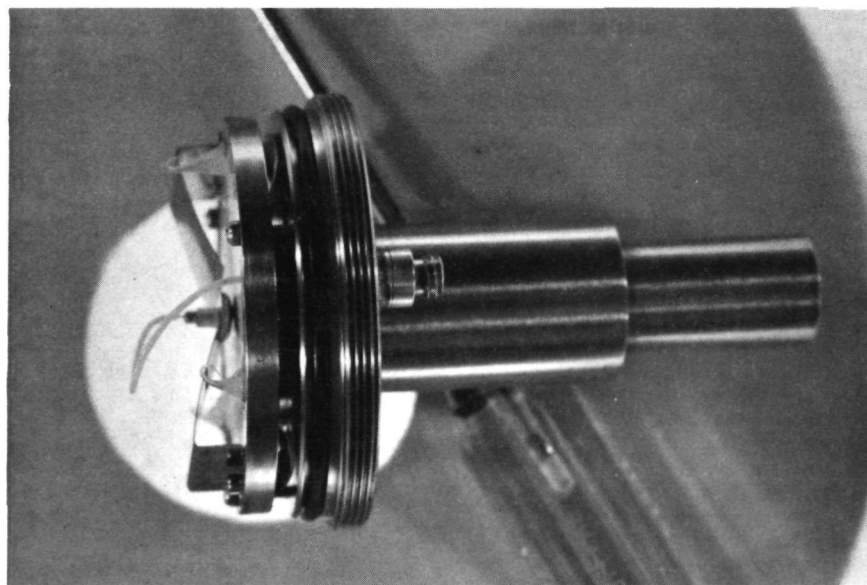
(b) Valve with cover removed

Fig. 7-1. Photographs of piezoelectric valve.
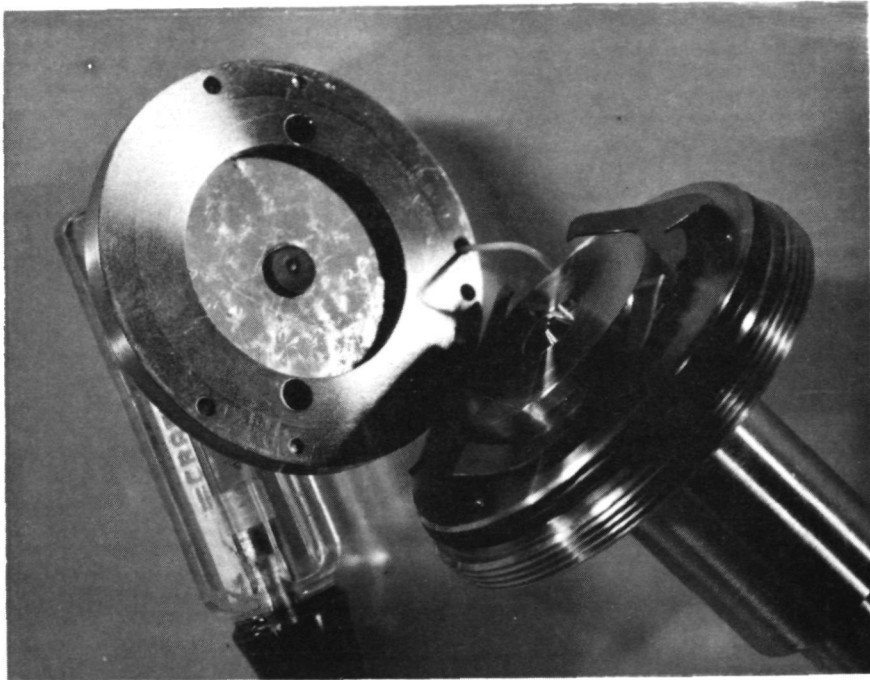
(c) Piezoelectric crystal lifted to show resilient
     pad and orifice

Fig. 7-1. Concluded.

Voltage controlled distortion of
crystal releieves pressure on resilient
pad fixed to bottom of crystal.

Gas
in

Gas
flow

Tapered
micro-groove

Piezoelectric crystal

(0-100 VDC)

Valve
body

Elec.
contact

Resilient pad

Gas flow orifice

Insulated
top mount

Gas
in

Gas
flow
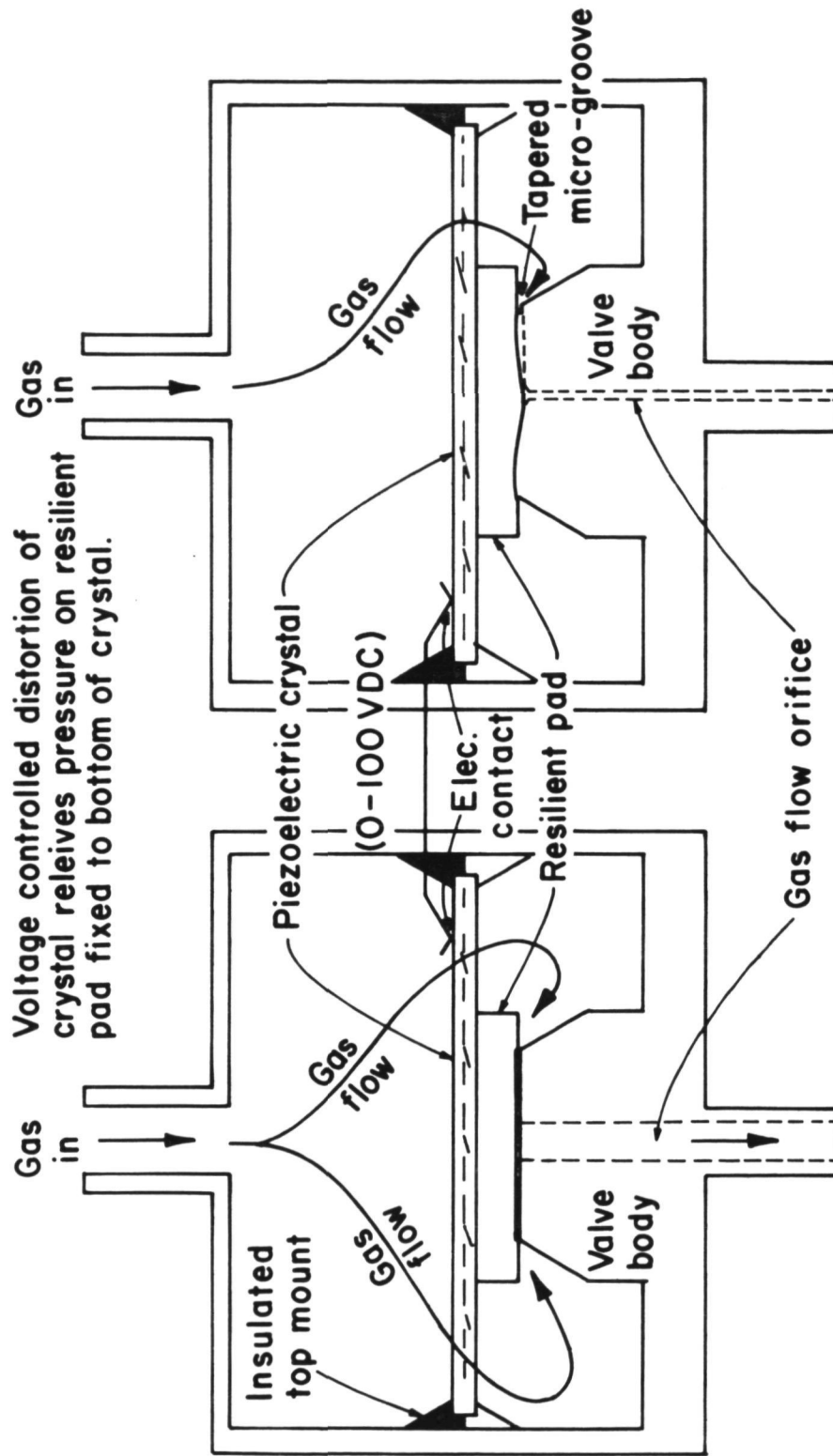
Valve
body

(a) Present design for pressure
regulation.

(b) Possible modification for more
sensitive flow control.

Figure 7-2.   Schematic representation of piezoelectric valve, together with possible
modification for more flow sensitivity.

to provide a positive shutoff. A voltage of 0-100 Vdc is applied to the top surface of the crystal, causing it to distort and (with sufficient voltage within this range) to relieve the preload pressure on the sealing pad, thereby permitting gas to flow. The control is sufficiently precise to permit setting of very low flow rates. The particular valve used herein began opening at about 37 Vdc, with full scale reached in an additional 2-3 V. The exact operating voltage varies several volts, depending on the differential pressure across the valve, the mechanical preload on the crystal, and temperature. Previous to two disassemblies, the operating range of the valve used centered around 70 V and 15 V, both with full control obtained over 2-3 V. The 0-100 V range specified by the manufacturer thus appears to include some tolerance for operating conditions, together with a larger tolerance for assembly. With only one moving part (the piezoelectric crystal with attached resilient pad), this type of valve appeared to have a high potential for reliability.

The flowmeter and valve described above were combined into a gas flow control shown in the block diagram of Fig. 7-3.* The power supply and control amplifier are shown in more detail in Figs. 7-4 and 7-5. The assembled flow control is shown in Fig. 7-6. In the electronic control loop (see Fig. 7-5), a voltage equivalent to the desired flow is set by adjusting R1. This voltage, after passing through an isolation amplifier,

---

* The piezoelectric valve is also used in a flow control by Veeco, but the sensing element used is an ion gauge instead of a thermocouple flowmeter. Because an ion gauge is much less stable and reproducible than a thermocouple flowmeter, the earlier flow control by Veeco was not considered for the application herein.
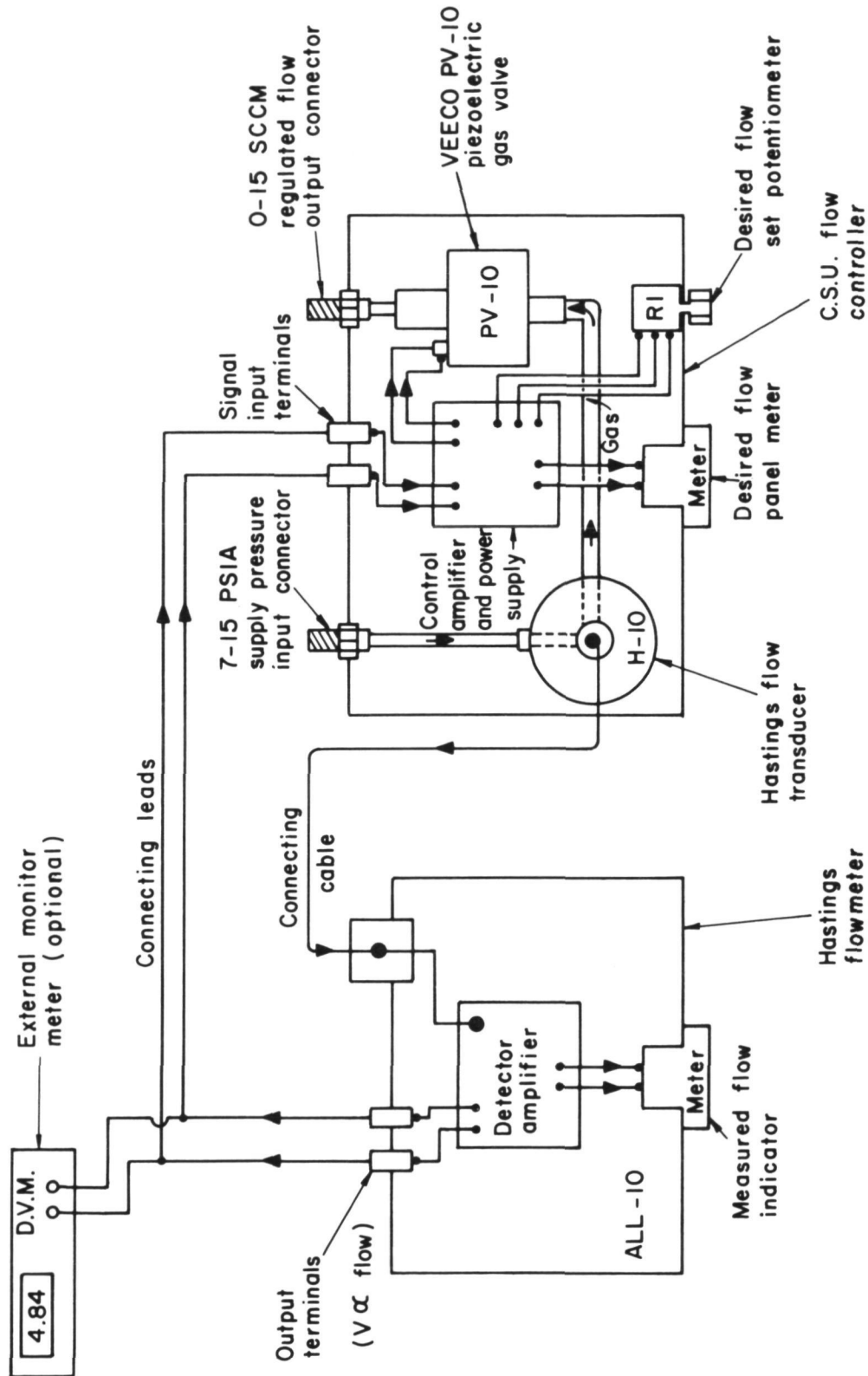
Figure 7-3. Block diagram of gas flow control.
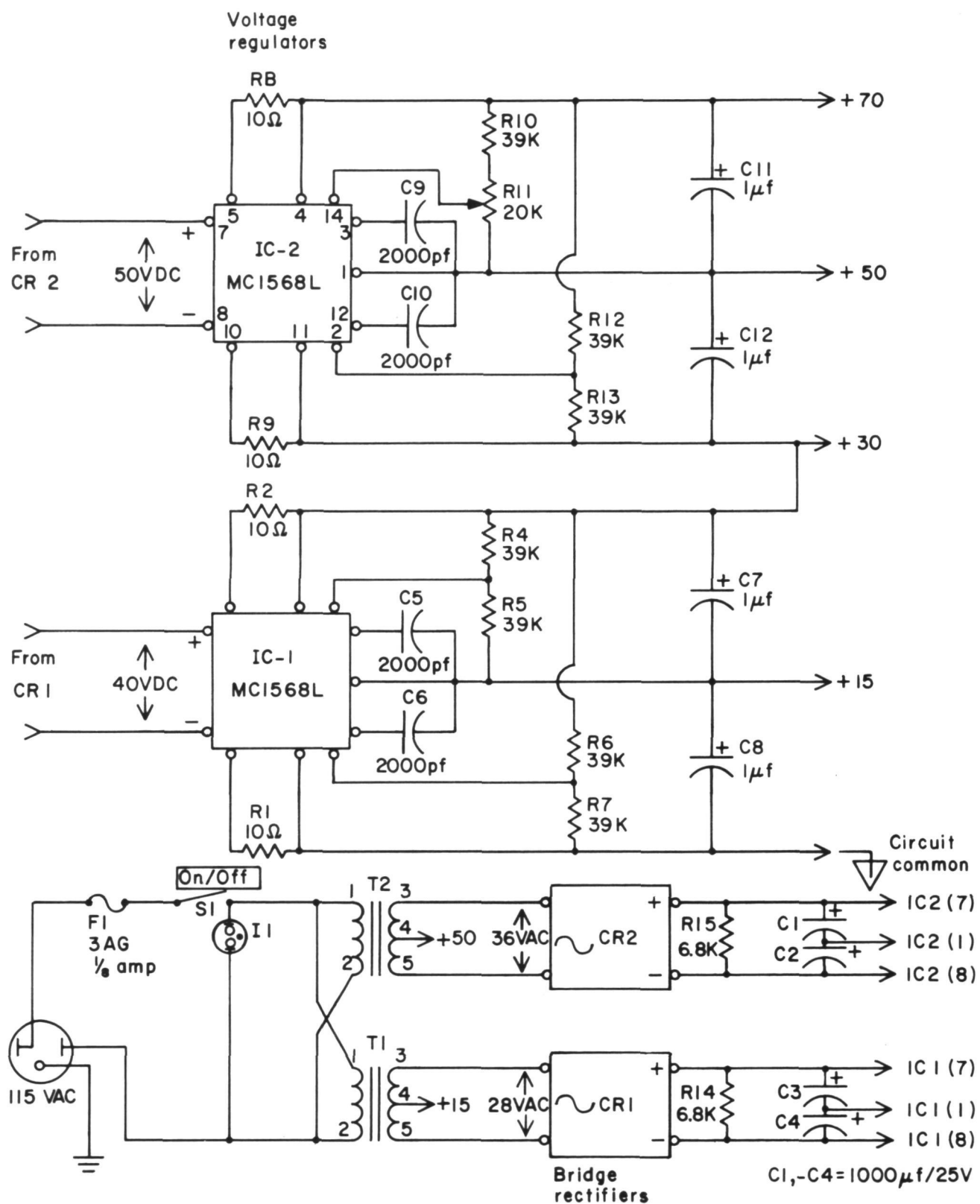
Figure 7-4. Schematic diagram of power supply for gas flow control.
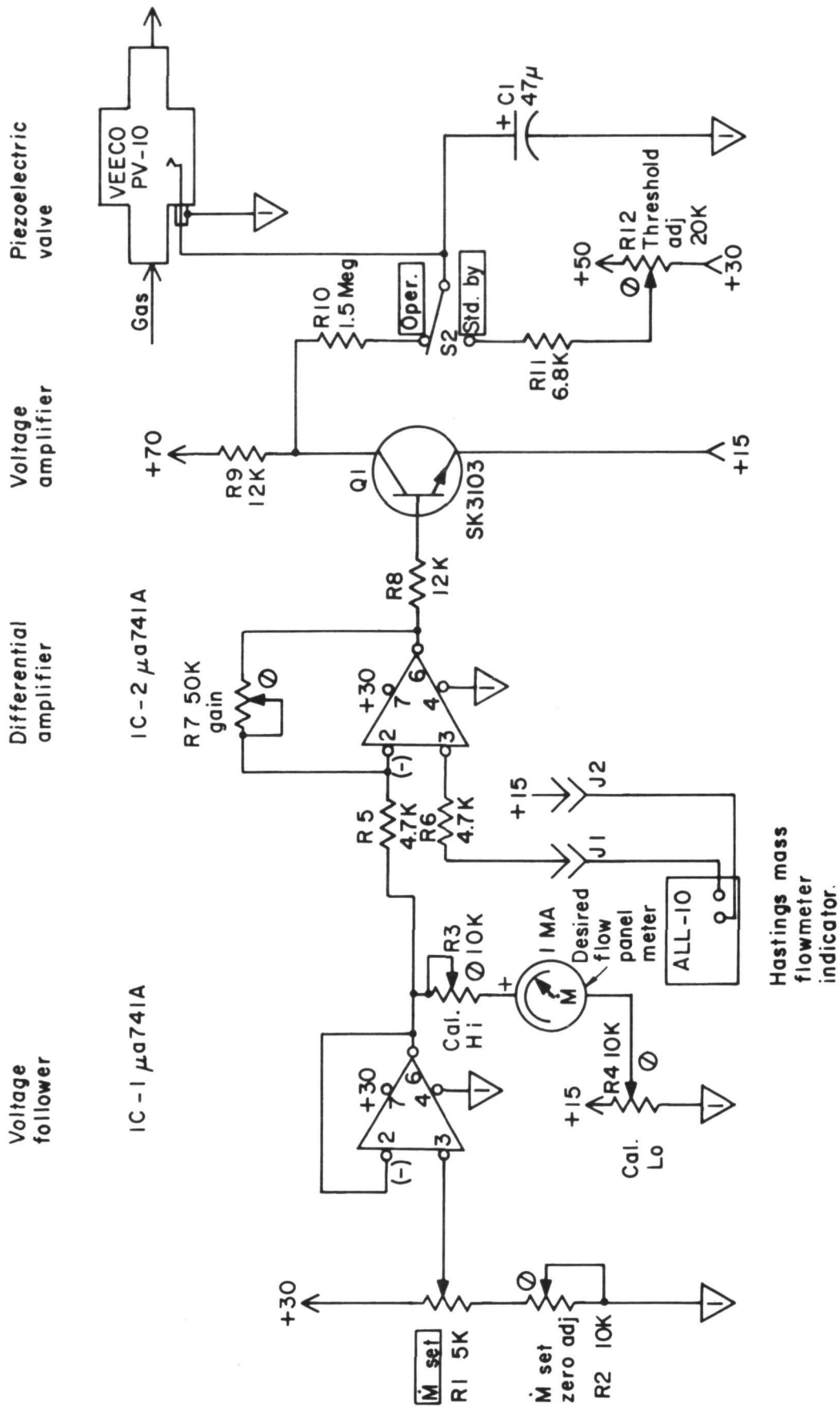
Figure 7-5. Schematic diagram of control amplifier for gas flow control.

(a) Front panel
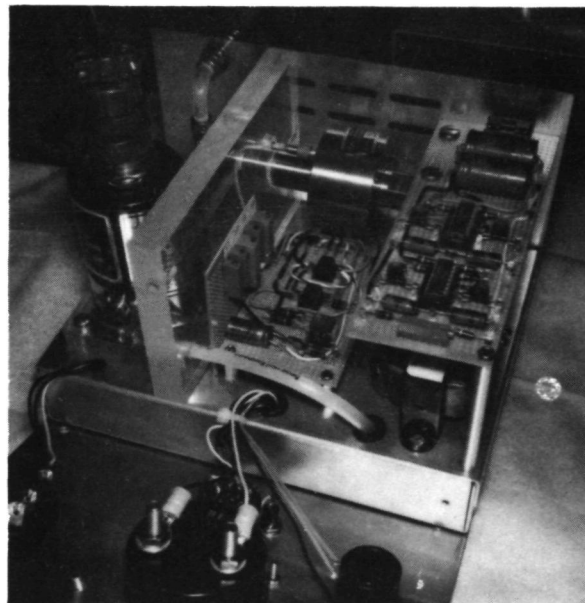
(b) With cover removed

Fig. 7-6. Photographs of assembled
flow control.

is applied to one input of the differential amplifier and to the "desired flow" panel meter. The voltage output of the flowmeter is applied to the other input of the differential amplifier, where the difference between the two voltages is the error signal that is amplified. After passing through the power amplifier (Q1), the error signal is used to control the piezoelectric valve. To damp out possible oscillations, an integrating circuit (R10 and C1) is used on the output of the power amplifier. To complete the control loop, the piezoelectric valve responds by changing the gas flow in the proper direction so that the output of the flowmeter is in closer agreement with the set voltage obtained from R1. At equilibrium, the circuit operates on a small error signal sufficient to compensate for any normal environmental or component variations.

The system specifications are essentially the combined specifications of the flowmeter and the piezoelectric valve. The directly indicated range of the flowmeter (by panel meter) is 0-10 sccm. Monitoring the output terminals on the back of the flowmeter permits this range to be extended to 0-15 sccm (approximate 0-1500 mA-equiv of Ar). The flowmeter accuracy is within 2% of full scale for the panel meter and within 1% of full scale when monitoring the voltage at the output terminals. The system will maintain the flow within 1% of the set point for 48 hours. With the flow into a near vacuum, variation of input pressure from 8-16 psia will not cause the 1% error to be exceeded. The ambient temperature can vary from 0-40°C without exceeding the same error. Operation for a fixed temperature within the -30 to +125°C range should be possible with recalibration, while operation over a wider input pressure range should be possible with a higher loop gain. The response rate of the system is essentially limited by the

flowmeter. The system will not track supply pressure change rates greater than about 0.1 psi/minute. After changing the set point, the flow was always stabilized within 3 minutes, usually in about 2 minutes. The power consumption is 15 W for the flowmeter and 6.5 W for the CSU controller.

Two aspects of this gas flow system would probably require study for flight applications. One would be the use of digital instead of analog logic to effectively remove the significance of any error signal in steady state operation. The other would be a thorough study of long term drift in the flowmeter calibration. Changes in environmental temperature, if significant, could probably be taken into account by a calibration of this effect. Other than the two aspects mentioned above, tests of the CSU gas flow control to date appear consistent with the eventual use of this approach in a flight application.

VIII   CONCLUDING REMARKS

Additional magnetic field measurements are reported herein. These measurements should be of use in magnetic field design.

The diffusion of electrons through the magnetic field above multipole anodes has been studied in detail. The data are consistent with Bohm diffusion across a magnetic field. The theory based on Bohm diffusion is simple and easily used for diffusion calculations.

Limited startup data were obtained for multipole discharge chambers. These data were obtained with refractory cathodes, but should be useful in predicting the upper limits for starting with hollow cathodes.

Discharge-chamber performance was obtained for a multipole discharge chamber operating with a hollow cathode. Discharge losses and utilizations were generally similar to those obtained with refractory cathodes, but the losses were 100-200 eV/ion lower. The higher losses with the refractory cathodes were believed due mostly to poor placement of these cathodes. The discharge voltage generally tended to decrease with either higher main-cathode flow rates or higher total discharge-chamber flow rates. These results are consistent with previous mercury-propellant experience. Limited doubly charged ion data were also obtained. To the extent that comparison was possible, these data were in agreement with similar data obtained with a refractory cathode.

Hollow cathode data were also obtained. These data indicated that in a bell jar the anode area is a more critical factor with argon and xenon than with mercury. Calculations of the ion drift with the neutral flow out a hollow cathode orifice support the viewpoint that ions are carried from the orifice against the local electric field by ion-atom collisions to the

plume region when operation is in the spot mode. A correlation parameter based on this picture has similarities to another correlation parameter derived previously.

A flow control is described in sufficient detail to permit duplication. The flowmeter and control valve used in this flow control both use concepts well suited for eventual development into space flight hardware.

REFERENCES

Section I

1. H. R. Kaufman, "Inert Gas Thrusters," NASA Contr. Rep. CR-135226, July 1977.

Section II

1. P. Lorrain and D. R. Corson, Electromagnetic Fields and Waves, 2nd ed., W. H. Freeman and Company, 1970, p. 411.

2. H. R. Kaufman, "Charge-Exchange Plasma Generated by an Ion Thruster," NASA Contr. Rep. CR-135318, Dec. 1977.

3. C. M. Haynes, "Fifteen cm Ion Source," in Industrial Ion Source Technology (H. R. Kaufman, ed.), NASA Contr. Rep. CR-135353, Nov. 1977, pp. 18-23.

4. H. R. Kaufman, "Industrial Ion Source Technology," NASA Contr. Rep. CR-135149, Nov. 1976.

Section III

1. D. Bohm, "Qualitative Description of the Arc Plasma in a Magnetic Field," in The Characteristics of Electrical Discharges in Magnetic Fields (A. Guthrie and R. K. Wakerling, eds.) McGraw-Hill Book Co., 1949, pp. 1-12.

2. L. Spitzer, Jr., Physics of Fully Ionized Gases, 2nd ed., Interscience Publishers, N.Y., 1962, pp. 47-48.

3. F. F. Chen, Introduction to Plasma Physics, Plenum Press, N.Y., 1974, p. 169.

4. R. S. Robinson, "Plasma Probe Measurements in the 30-cm Discharge Chamber," in Industrial Ion Source Technology (H. R. Kaufman, ed.), NASA Contr. Rep. CR-135353, Nov. 1977, pp. 3-17.

5. R. S. Robinson, "Thirty cm Ion Source," in Industrial Ion Source Technology (H. R. Kaufman, ed.), NASA Contr. Rep. CR-135149, Nov. 1976, pp. 1-59.

6. G. C. Isaacson, "Multipole Gas Thruster Design," <u>NASA Contr. Rep.</u> CR-135101, June 1977, pp. 45-51.

7. R. D. Moore, "Magneto-Electrostatically Contained Plasma Ion Thruster," <u>AIAA Paper</u> 69-260, March 1969.

8. W. D. Ramsey, "12-cm Magneto-Electrostatic Containment Mercury Ion Thruster Development," <u>J. Space. Rockets</u>, Vol. 9, May 1972, pp. 318-321.

9. C. M. Haynes, "Fifteen cm Ion Source," in Industrial Ion Source Technology," (H. R. Kaufman, ed.), <u>NASA Contr. Rep.</u> CR-135353, Nov. 1977, pp. 18-23.

10. H. R. Kaufman, "Charge-Exchange Plasma Generated by an Ion Thruster," <u>NASA Contr. Rep.</u> CR-135318, Dec. 1977.

Section IV

1. H. R. Kaufman, "Charge-Exchange Plasma Generated by an Ion Thruster," <u>NASA Contr. Rep.</u> CR-135318, Dec. 1977.

2. C. M. Haynes, "Fifteen cm Ion Source," in <u>Industrial Ion Source Technology</u>, (H. R. Kaufman, ed.), <u>NASA Contr. Rep.</u> CR-135353, Nov. 1977, pp. 18-23.

3. H. R. Kaufman, "Industrial Ion Source Technology," <u>NASA Contr. Rep.</u> CR-135149, Nov. 1976.

Section V

1. H. R. Kaufman, "Experimental Investigations of Argon and Xenon Ion Sources," NASA Contr. Rep. CR-134845, June 1975.

2. H. R. Kaufman, "Inert Gas Thrusters," <u>NASA Contr. Rep.</u> CR-135100, July 1976.

3. H. R. Kaufman, "Multipole Gas Thruster Design," <u>NASA Contr. Rep.</u> CR-135101, June 1977.

4. H. R. Kaufman, "Inert Gas Thrusters," <u>NASA Contr. Rep.</u> CR-135226, July 1977.

5. R. D. Moore, "Magneto-Electrostatically contained Plasma Ion Thruster," AIAA Paper No. 69-260, March 1969.

6. W. Ramsey, "12-cm Magneto-Electrostatic Containment Mercury Ion Thruster Development," J. Space. Rockets, Vol. 9, May 1972, pp. 318-321.

Section VI

1. H. R. Kaufman, "Inert Gas Thrusters," NASA Contr. Rep. CR-135226, July 1977.

2. J. D. Cobine, Gaseous Conductors, Dover Publications, New York, 1958, pp. 246-247.

3. G. S. Anderson, "Hg Adsorption Studies Using Atom Ejection Patterns," J. Appl. Physics, Vol. 36, May 1965, pp. 1558-1561.

4. D. S. Newsome, "Significant Structure Theory of Multilayer Physical Adsorption," J. Physical Chemistry, Vol. 78, 1974, pp. 2600-2604.

5. S. Dushman, Scientific Foundations of Scientific Technique, John Wiley & Sons, New York, 1949, p. 36.

6. D. E. Siegfried and P. J. Wilbur, "An Investigation of Mercury Hollow Cathode Phenomena," AIAA Paper 78-705, April 1978.

7. H. R. Kaufman, "Technology of Electron-Bombardment Ion Thrusters," in Advances in Electronics and Electron Physics, Vol. 36 (ed., L. Marton), Academic Press, New York, 1974.

Section VII

1. Teledyne Hastings-Raydist, Hampton, Virginia 23661.

2. Veeco Instruments, Inc., Terminal Drive, Plainview, New York 11803.

DISTRIBUTION LIST

National Aeronautics and Space Administration
Washington, DC 20546
Attn: RPE/Mr. Wayne Hudson   1
       Mr. Daniel H. Herman, Code SL   1

National Aeronautics and Space Administration
Lewis Research Center
21000 Brookpark Road
Cleveland, OH 44135
Attn: Research Support Procurement Section
       Mr. Allen Jones, MS 500-313   1
       Technology Utilization Office, MS 3-19   1
       Report Control Office, MS 5-5   1
       Library, MS 60-3   2
       N. T. Musial, MS 600-113   1
       Spacecraft Technology Division, MS 501-8
         Mr. H. Douglass   1
         Mr. R. Finke   1
         Mr. D. Byers   1
         Mr. B. Banks   1
         Mr. S. Domitz   1
         Mr. F. Terdan   1
         Mr. W. Kerslake   1
         Mr. Vincent K. Rawlin   20
         Mr. M. Mirtich   1
       Physical Science Division, MS 301-1
         Mr. W. E. Moeckel   1

National Aeronautics and Space Administration
Marshall Space Flight Center
Huntsville, AL 35812
Attn: Mr. Jerry P. Hethcoate   1

Research and Technology Division
Wright-Patterson AFB, OH 45433
Attn: (ADTN) Lt. David A. Fromme   1

NASA Scientific and Technical Information Facility
P. O. Box 8757
Baltimore/Washington International Airport
Baltimore, MD 21240   40

Case Western Reserve University
10900 Euclid Avenue
Cleveland, OH 44106
Attn: Dr. Eli Reshotko   1

Royal Aircraft Establishment
Space Department
Farnborough, Hants, ENGLAND
Attn: Dr. D. G. Fearn   1

United Kingdom Atomic Energy Authority
Culham Laboratory
Abingdom, Berkshire, ENGLAND
Attn: Dr. P. J. Harbour   1
        Dr. M. F. A. Harrison   1
        Dr. T. S. Green   1

National Aeronautics and Space Administration
Goddard Space Flight Center
Greenbelt, MD 20771
Attn: Mr. W. Isley, Code 734   1
        Mr. R. Bartlett, Code 713   1
        Mr. R. Callens, Code 734   1

SAMSO
Air Force Unit Post Office
Los Angeles, CA 90045
Attn: Capt. D. Egan/ SYAX   1

Comsat Laboratories
P. O. Box 115
Clarksburg, MD 20734
Attn: Mr. B. Free   1
        Mr. O. Revesz   1

Roket Propulsion Laboratory
Edwards AFB, CA 93523
Attn: LKDA/Ms. Tom Waddell   2

DFVLR - Institut für Plasmadynamik
Technische Universitat Stuttgart
7 Stuttgart-Vaihingen
Allmandstr 124
WEST GERMANY
Attn: Dr. G. Krülle   1

Giessen University
1st Institute of Physics
Geissen, WEST GERMANY
Attn: Professor H. W. Loeb   1

Jet Propulsion Laboratory
4800 Oak Grove Drive
Pasadena, CA 91102
Attn: Dr. Kenneth Atkins   1
        Technical Library   1
        Mr. Eugene Pawlik   1
        Mr. James Graf   1

Electro-Optical Systems, Inc.
300 North Halstead
Pasadena, CA 91107
Attn: Mr. R. Worlock   1
        Mr. E. James   1
        Mr. W. Ramsey   1

TRW, Inc.
TRW Systems
One Space Park
Redondo Beach, CA 90278
Attn: Mr. M. Huberman   1

       Dr. S. Zafran   1

National Aeronautics and Space Administration
Ames Research Center
Moffett Field, CA 94035
Attn: Technical Library   1

National Aeronautics and Space Administration
Langley Research Center
Langley Field Station
Hampton, VA 23365
Attn: Technical Library   1

Hughes Research Laboratories
3011 Malibu Canyon Road
Malibu, CA 90265
Attn: Dr. Jay Hyman   1
       Mr. J. H. Molitor   1
       Dr. R. L. Poeschel   1
       Mr. R. Vahrenkamp   1
       Dr. John R. Beattie   1

United States Air Force
Office of Scientific Research
Washington, DC 20025
Attn: Mr. M. Slawsky   1

Princeton University
Princeton, NJ 08540
Attn: Mr. W. F. Von Jaskowsky   1
       Dean R. G. Jahn   1
       Dr. K. E. Clark   1

Communications Research Centre
Ottawa, Ontario, CANADA
Attn: Dr. W. F. Payne   1

Joint Institute for Laboratory Astrophysics
University of Colorado
Boulder, CO 80302
Attn: Dr. Gordon H. Dunn   1

Department of Aeronautics and Astronautics
Stanford University
Stanford, CA 94305
Attn: Professor Howard S. Seifert   1

Boeing Aerospace Company
P. O. Box 3999
Seattle, WA 98124
Attn: Mr. Donald Grim   1

Intelcom Rad Tech
7650 Convoy Court
P. O. Box 80817
San Diego, CA 92138
Attn: Dr. David Vroom   1

Lockheed Missiles and Space Company
Sunnyvale, CA 94088
Attn: Dr. William L. Owens
       Propulsion Systems, Dept. 62-13   1

Fairchild Republic Company
Farmingdale, NY 11735
Attn: Dr. William Guman   1

COMSAT Corporation
950 L'Enfant Plaza S.W.
Washington, DC 20024
Attn: Mr. Sidney O. Metzger   1

Electrotechnical Laboratory
Tahashi Branch
5-4-1 Mukodai-Machi, Tanashi-Shi
Tokyo, JAPAN
Attn: Dr. Katsuva Nakayama   1

Office of Assistant for Study Support
Kirtland Air Force Base
Albuquerque, NM 87117
Attn: Dr. Calvin W. Thomas OAS Ge   1
       Dr. Berhart Eber OAS Ge   1

Bell Laboratories
600 Mountain Avenue
Murray Hill, NJ 07974
Attn: Dr. Edward G. Spencer   1
       Dr. Paul H. Schmidt   1

Massachusetts Institute of Technology
Lincoln Laboratory
P. O. Box 73
Lexington, MA 02173
Attn: Dr. H. I. Smith   1

Sandia Laboratories
Mail Code 5742
Albuquerque, NM 87115
Attn: Mr. Ralph R. Peters   1

Service du Confinement des Plasma
Centre d'Etudes Nucléaires - F.A.R.
B.P. 6
92260 Fontenay-aux-Roses
FRANCE
Attn: Dr. J. F. Bonal   1

International Business Machines Corporation
Thomas J. Watson Research Center
P. O. Box 218
Yorktown Heights, NY 10598
Attn: Dr. Jerome J. Cuomo   1
       Dr. James M. E. Harper   1

IBM East Fishkill
D/42K, Bldg. 300-40F
Hopewell Junction, NY 12533
Attn: Dr. Charles M. McKenna   1

DFVLR-Forschungszentrum Braunschweig
Inst. A, Flughafen
3300 Braunschweig
WEST GERMANY
Attn: Dr. H. A. W. Bessling   1

Ion Beam Equipment, Inc.
P. O. Box O
Norwood, NJ 07648
Attn: Dr. W. Laznovsky   1

Optic Electronics Corporation
11477 Pagemill Road
Dallas, TX 75243
Attn: Bill Hermann, Jr.   1

Circuits Processing Apparatus, Inc.
725 Kifer Road
Sunnyvale, CA 94086
Attn: Spencer R. Wilder   1

Ion Tech, Inc.
1807 E. Mulberry
P. O. Box 1388
Fort Collins, CO 80522
Attn: Dr. Gerald C. Isaacson   1

Physicon Corporation
221 Mt. Auburn Street
Cambridge, MA 02138
Attn: H. von Zweck   1

Commonwealth Scientific Corporation
500 Pendleton Street
Alexandria, VA 22314
Attn: George R. Thompson   1

Veeco Instruments Inc.
Terminal Drive
Plainview, NY 11803
Attn: Norman Williams   1